Synaptic inputs to motor neurons underlying muscle coactivation for functionally different tasks have different spectral characteristics

J Neurophysiol 131: 1126–1142, 2024.
First published April 17, 2024; doi:10.1152/jn.00199.2023

american physiological society

JNP JOURNAL OF NEUROPHYSIOLOGY

RESEARCH ARTICLE

Control of Movement

Synaptic inputs to motor neurons underlying muscle coactivation for functionally different tasks have different spectral characteristics

Daniele Borzelli,[1,2] Taian M. M. Vieira,[3,4] Alberto Botter,[3,4] Marco Gazzoni,[3,4] Francesco Lacquaniti,[2,5] and Andrea d'Avella[1,2]

[1]*Department of Biomedical, Dental, Morphological and Functional Imaging Sciences, University of Messina, Messina, Italy;* [2]*Laboratory of Neuromotor Physiology, IRCCS Santa Lucia Foundation, Rome, Italy;* [3]*Laboratory for Engineering of the Neuromuscular System, Department of Electronics and Telecommunications, Politecnico di Torino, Turin, Italy;* [4]*PoliToBIOMed Lab, Politecnico di Torino, Turin, Italy; and* [5]*Department of Systems Medicine and Center of Space BioMedicine, University of Rome Tor Vergata, Rome, Italy*

Abstract

The central nervous system (CNS) may produce the same endpoint trajectory or torque profile with different muscle activation patterns. What differentiates these patterns is the presence of cocontraction, which does not contribute to effective torque generation but allows to modulate joints' mechanical stiffness. Although it has been suggested that the generation of force and the modulation of stiffness rely on separate pathways, a characterization of the differences between the synaptic inputs to motor neurons (MNs) underlying these tasks is still missing. In this study, participants coactivated the same pair of upper-limb muscles, i.e., the biceps brachii and the triceps brachii, to perform two functionally different tasks: limb stiffness modulation or endpoint force generation. Spike trains of MNs were identified through decomposition of high-density electromyograms (EMGs) collected from the two muscles. Cross-correlogram showed a higher synchronization between MNs recruited to modulate stiffness, whereas cross-muscle coherence analysis revealed peaks in the β-band, which is commonly ascribed to a cortical origin. These peaks did not appear during the coactivation for force generation, thus suggesting separate cortical inputs for stiffness modulation. Moreover, a within-muscle coherence analysis identified two subsets of MNs that were selectively recruited to generate force or regulate stiffness. This study is the first to highlight different characteristics, and probable different neural origins, of the synaptic inputs driving a pair of muscles under different functional conditions. We suggest that stiffness modulation is driven by cortical inputs that project to a separate set of MNs, supporting the existence of a separate pathway underlying the control of stiffness.

NEW & NOTEWORTHY The characterization of the pathways underlying force generation or stiffness modulation are still unknown. In this study, we demonstrated that the common input to motor neurons of antagonist muscles shows a high-frequency component when muscles are coactivated to modulate stiffness but not to generate force. Our results provide novel insights on the neural strategies for the recruitment of multiple muscles by identifying specific spectral characteristics of the synaptic inputs underlying functionally different tasks.

beta rhythm; cocontraction; common drive; high-density electromyography; motor unit

INTRODUCTION

The musculoskeletal system, owing to its redundancy (1), may produce the same joint trajectory or torque profile with a multitude of combinations of muscle activation patterns differing in the amount of cocontraction. In other words, the coactivation of muscles generating torques with opposite signs at a given joint will not contribute to end point force, but will help modulating stiffness at that joint (2, 3). In turn, stiffness modulation can reduce the effect of external perturbations (4–6), for instance by stabilizing the limb during ball catching (7) and improving accuracy of arm movement control (8–10).

How the central nervous system (CNS) regulates cocontraction is still not fully understood, despite the generally

Correspondence: D. Borzelli (daniele.borzelli@unime.it).
Submitted 15 May 2023 / Revised 11 April 2024 / Accepted 11 April 2024

acknowledged role in stiffness control and the recent interest in the mechanisms of recruitment of motor units in antagonist muscles during different tasks (11). Several studies support the hypothesis that separate control mechanisms underlie the generation of force or the modulation of stiffness (5, 12–16). However, a characterization of the distinctive spectral properties of the synaptic input driving stiffness modulation, with respect to the synaptic input involved in the generation of force, is still missing. The spectral properties of the synaptic inputs to α motoneurons are important, in so far as they can be related to the neural substrates potentially driving motoneurons activation (17).

It is well established that the common synaptic input within a given motor neuron (MN) pool, which determines the muscle force (17), can be identified using coherence analysis on the trains of action potentials of pairs of MNs (18). Recently, coherence analysis has also been used to assess the synchronous modulation of separate neural drives to MN pools, identified through high-density electromyograms (EMGs) and a validated decomposition approach (19–21), to unveil the synaptic inputs shared across muscles (22–24). However, despite coherence analysis would also allow to discern the occurrence of a common input to a pair of antagonist muscles during a cocontraction task, a functional characterization of the spectral features underlying the modulation of limb stiffness also requires a control condition in which the same pair of antagonist muscles are coactivated to exert a force along a direction that none of them can generate, rather than to modulate stiffness.

Studies investigating the common drive to pairs of muscles during a stiffness modulation task (25–27) and during a force generation task (25, 28, 29) examined different muscle pairs in different tasks. Thus, the observation of different spectral features may be related to the different properties of the muscles rather than to the characteristics of different synaptic inputs underlying the two tasks. Importantly, to assess two distinct functions associated with the coactivation of a pair of muscles that have an antagonistic action at one joint, it is necessary to consider pairs of muscles acting on multiple joints. Although the actions of the two muscles may be antagonistic at one joint, i.e., they may generate torques with opposite sign that cancel each other, their action at other joints may not be antagonistic. Thus, their coactivation in the context of a multi-articular system may be useful to generate a net end point force in a specific direction. Therefore, to disentangle different functional roles of coactivation it is necessary to use an experimental paradigm involving a pair of muscles acting on multiple joints, and comparing one task in which coactivation generates no net force but increases stiffness, and a second task in which coactivation generates a net force.

In this study, we designed an innovative experimental paradigm, which exploited the anatomical properties of the upper limb to characterize the common input to a pair of muscles, i.e., the biceps brachii (BB) and the triceps brachii (TB). As BB acts both as elbow flexor and wrist supinator, the coactivation of BB and TB may underlie two functionally different tasks: the modulation of upper limb stiffness and the generation of an end point force. We asked participants to control the displacement of a cursor in a tridimensional virtual space by exerting isometric end point forces. The horizontal displacement was achieved by the exertion of forces along the horizontal plane, whereas the vertical displacement was achieved by the exertion of a supination torque by the wrist. In this condition, the coactivation of BB and TB was required to generate a joint torque. In contrast, during a second experimental condition, participants were instructed to voluntarily cocontract their muscles to compensate the oscillation of the cursor around a mean position, i.e., regulating a "virtual stiffness" (12, 30), while still trying to reach targets that lied on the horizontal plane by exerting isometric forces. Therefore, in this condition coactivation (or cocontraction) of BB and TB was aimed at modulating stiffness.

First, the spike trains of MNs were identified by decomposing high-density surface electromyograms (HDsEMGs) recorded from BB and TB muscles during these tasks. We then performed two analyses on the spike trains: cross-correlation and coherence. These two analyses provide complementary information on the common input driving the pools of MNs identified on the two muscles. In fact, although the cross-correlogram provides the temporal coupling between the two signals, the coherence measures their common frequency contents. Since the synaptic input that modulates limb stiffness was suggested to originate at the cortical level (13, 14), we hypothesized a higher synchronization and a β-band peak in the coherence between the spike trains of the MN pools identified on the BB and on the TB when the two muscles cocontracted to modulate the stiffness (see Fig. 1*C*), but not when they were coactivated to generate an end point force (see Fig. 1*D*). In fact, previous studies on corticomuscular coherence demonstrated the occurrence of a β band (15–30 Hz) peak during isometric tasks (31), deriving from the rhythmic discharges in the corticospinal neurons projecting to the spinal motoneurons (32). Therefore, in the literature, this frequency component of the synaptic input to a MN pool has been commonly interpreted as being of cortical origin (17). Since we implemented the same method introduced by Laine et al. (23), our results on antagonist muscles could be directly compared with their results on synergistic muscles. This would provide a wider description of the spectral components of the common input shared between different pairs of muscles under different conditions.

We also assessed the coherence of the spike trains of MNs of each muscle after removing the common input to the antagonist muscle or related to the exerted force. Such residual coherence (23) allows to distinguish MNs selectively recruited to modulate stiffness from those involved in force generation, and therefore to characterize the spectral properties of the synaptic input that drives these MN pools. The identification of MN subsets that were selectively driven to control force or cocontraction though synaptic inputs with different spectral characteristics supports the existence of specific neural pathways that control the two functionally different tasks.

To the best of our knowledge, our results provide the first evidence that muscles involved in different tasks are driven by synaptic inputs showing different spectral characteristics, and demonstrate the existence of a population of MNs that are selectively recruited to modulate stiffness.

MATERIALS AND METHODS

Eight healthy male adults (age range: 22–35 yr) participated in the study after giving written informed consent. All participants were right-handed, as assessed according to the

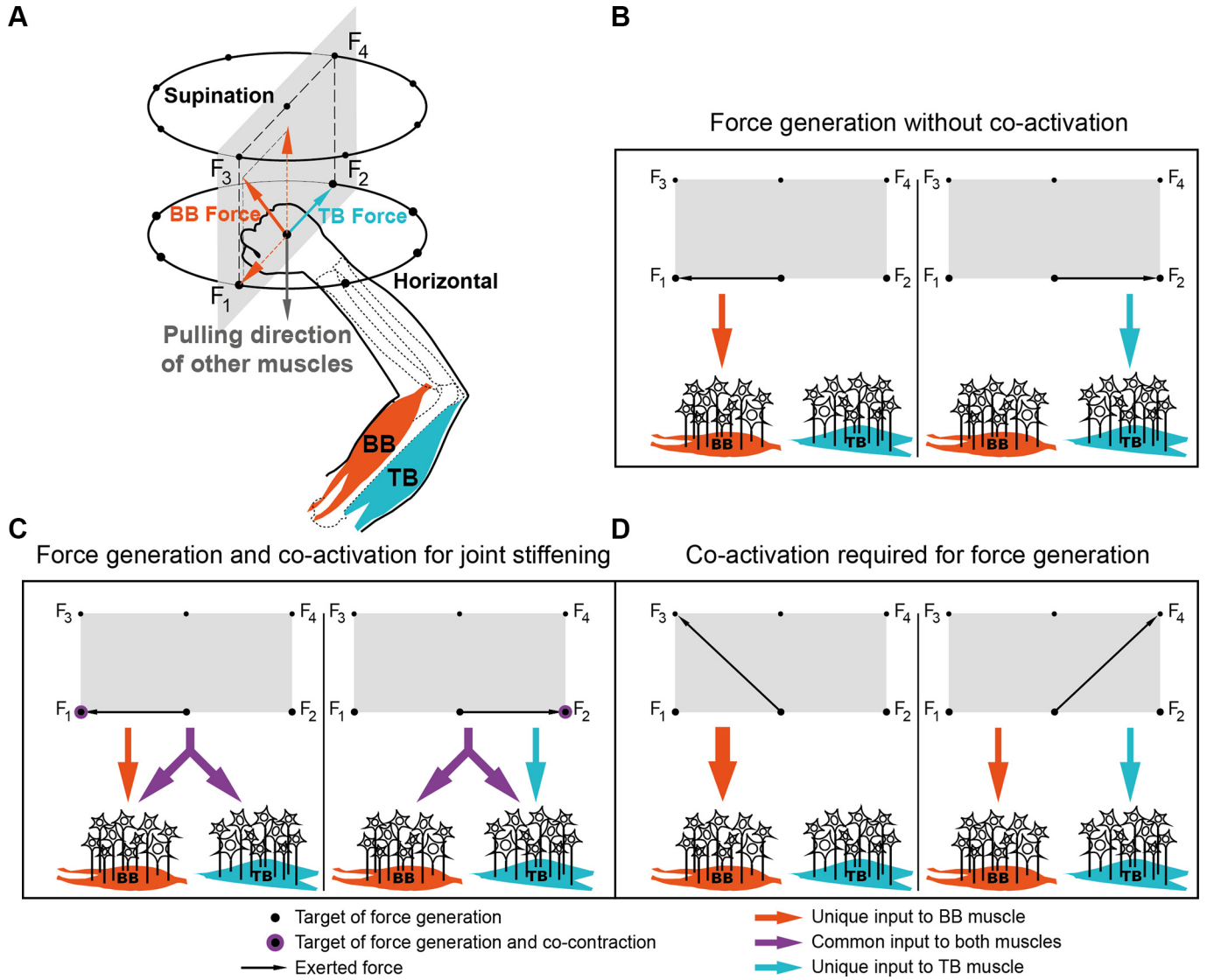

Figure 1. Conceptual models of synaptic inputs to motor neurons for the generation of force and the modulation of cocontraction. *A*: an upper-limb task designed to dissociate coactivation of antagonist muscles for impedance modulation and for force generation. Force targets (black dots) arranged in two parallel planes can be reached by applying different combinations of torques at the upper-limb joints. Horizontal targets in the lower plane can be reached by different combinations of shoulder and elbow flexion or extension torques, producing horizontal forces at the hand. Supination targets in the higher plane require the combination of shoulder and elbow torques (horizontal force) with wrist supination torque (producing a torque at the hand mapped as vertical displacement in this task). Two muscles are considered: triceps brachii (TB), an elbow extensor, i.e., with a pulling vector (cyan arrow) in the horizontal plane (toward target F2), and biceps brachii (BB), whose action is both elbow flexion and forearm supination, i.e., with a pulling vector (red arrow) that has both a component (dashed arrows) in the Horizontal plane (toward target F1, opposite to TB) and a vertical component, required to reach the Supination plane. Thus, the coactivation of BB and TB may result in two actions, depending on the activation of other muscles (gray downward arrow in *A*): the increase of the elbow impedance through cocontraction with zero resultant force, or the simultaneous exertion of an endpoint force and supination torque. Four targets are highlighted: F1 and F2, lying on the Horizontal plane and requiring, respectively, an elbow flexion or an elbow extension torque to be reached, and F3 and F4, lying on the Supination plane and requiring wrist supination torque combined with, respectively, an elbow flexion or an elbow extension torque. *B*: targets F1 or F2 requires separate synaptic inputs to motor neuron (MN) pools of BB (red arrow) or TB (cyan arrow). *C* and *D*: synaptic inputs to MN pools of BB and TB during different tasks. A specific shared common input to control impedance by cocontraction (violet arrows) would be active during Horizontal force generation with cocontraction modulation (*C*) but not during Supination force generation without cocontraction modulation (*D*).

preferred hand used to perform common tasks (e.g., writing, throwing a ball, shaving). All participants had normal or corrected to normal vision and did not report having had any neurological disorder or upper right limb injury. The novelty of the approach did not allow to perform a power analysis, so the number of participants was selected in line with previous studies with a similar protocol and aim (23, 24, 33, 34). All procedures were conducted in accordance with the Declaration of Helsinki and were approved by the ethics committee IRCCS Sicilia-Sezione Neurolesi "Bonino-Pulejo" (Prot. No. 02/18).

Setup

Participants sat on a gaming chair in front of a desktop with car safety belts immobilizing their torso and shoulders (see Fig. 2*A*). The right hand was fully pronated and inserted

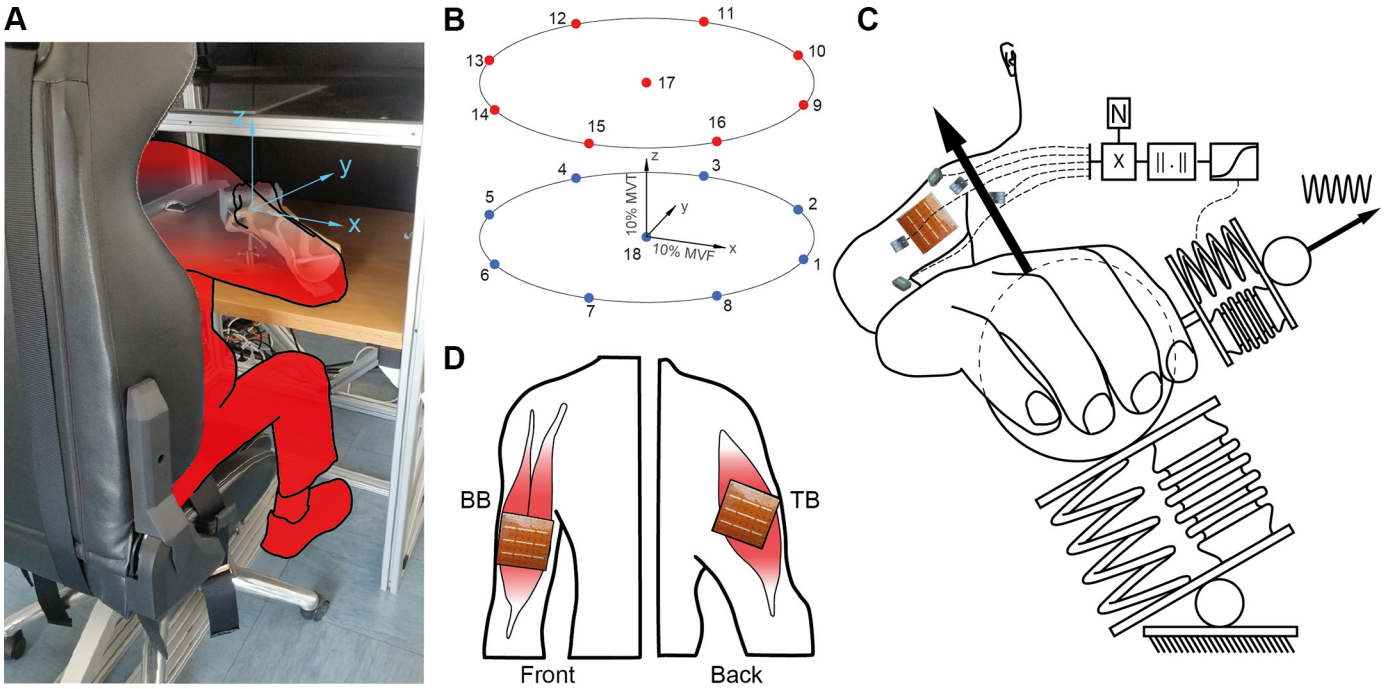

Figure 2. Experimental setup. *A*: participants inserted their right forearm into an orthosis rigidly connected to a six-axis force transducer, fixed below a desktop. Participant viewed a virtual scene that consisted of a spherical cursor whose displacement from the rest position (i.e., the position that the cursor assumed when the muscles were relaxed) was proportional to the exerted force and torque. The origin of the coordinate system used to displace the cursor in the virtual scene was placed at the center of the participant's palm. Participants could move the cursor in the horizontal plane by exerting horizontal forces (*x*-axis: medio-lateral direction; *y*-axis: dorso-ventral direction), and along the vertical direction (*z*-axis: upward vertical direction) exerting a forearm supination torque. *B*: participants were instructed to displace the cursor to reach one of 18 spherical targets arranged in two parallel horizontal (*x*-*y*) planes. Horizontal targets (blue) lay in the lower horizontal plane and Supination targets (red) lay in the upper horizontal plane and required a supination torque to be reached. *C*: during Perturbation blocks, the motion of the cursor was simulated as two mass-spring-damper systems (MSDs) in series. The first MSD was displaced by the force exerted by the participant, recorded by the force transducer, and determined the mean position of the cursor. The second MSD was perturbed by a simulated external unpredictable force and determined the oscillations around the mean position. Participant could reduce the magnitude of the oscillations of the second MSD system in real-time by voluntarily cocontracting their muscles. *D*: high-density electromyogram (EMG) grids covered the biceps brachii (BB, *left*) and triceps brachii (TB) lateral head (*right*) muscles.

in an orthosis, rigidly connected to a cylindrical handle that participants could grasp to easily generate supination torques, and to a six-axis force transducer (Delta F/T Sensor, ATI Industrial Automation, Apex, NC). The height of the chair and its distance from the table were set to ensure the elbow angle was 90° (0° full extension) and the hand was at the height of the solar plexus. Therefore, the shoulder roughly assumed a rotation angle of 60°, an abduction angle of 65°, and an extension angle of 55°. A horizontal mirror, preventing the view of the participant's hand, reflected the image displayed by a monitor rendered at 120 Hz (60 Hz per eye). Participants wore shutter glasses (GeForce 3-D Vision 2, NVIDIA Corporation, Santa Clara, CA) that allowed the stereoscopic vision of a three-dimensional scene. The scene comprised a desktop and a cursor whose displacement was computed in real time from the measured isometric force and torque and from surface EMGs collected with bipolar electrodes on multiple muscles acting on the elbow and shoulder joints (see *Bipolar Surface Electromyography*). At rest, and without perturbing forces, the cursor was displayed at a position corresponding to the center of the palm (rest position). The displacement in the horizontal plane was proportional to the force generated in the horizontal plane, whereas the vertical displacement was proportional to the supination torque.

Experimental Design

After an initial familiarization phase, participants performed three blocks of trials. In the first block, denoted maximal voluntary force and torque (MVFT) block, they were asked to exert their maximum voluntary force (MVF) and maximum voluntary torque (MVT). The MVF was the maximum force that participants could generate toward their chest along the horizontal plane ($-y$ direction; Fig. 2*A*) and the MVT was the maximum torque that participants could generate supinating their wrist ($+z$ direction). Participants alternated two repetitions of MVF with two repetitions of MVT and the peak values were used to normalize the target positions in the following blocks (MVF normalized the position along the horizontal *x*-*y* plane, MVT normalized the target position along the vertical *z* axis). The second block (Baseline) was composed of 17 trials during which participants were asked to move a spherical cursor from the rest position to a target position, located in one of 17 spatial positions (see Fig. 2*B*). Similarly, the third block (Perturbation) was composed of 18 trials during which participants were asked to stabilize the cursor in the rest position by increasing muscular cocontraction, or to move it from the rest position to a target position, located in one of the 17 spatial positions also used in the Baseline block. At the beginning of each trial (rest phase), participants were asked to relax their right arm

muscles to maintain the cursor inside a semitransparent sphere in the rest position. After doing so for 1 s, the sphere disappeared and reappeared in one of the target positions (target go event). One subset of targets included eight targets equally spaced along a circumference in the horizontal plane with 20% MVF radius (targets 1 to 8 in Fig. 2*B*), together with the target in the rest position (target 18, only in Perturbation block). No supination torque was required to reach this set of horizontal targets. The other subset included 9 targets at the same horizontal positions but with an offset of 20% MVT in the $+z$ direction (targets 9–17 in Fig. 2*B*). These supination targets could be reached only by eliciting a 20% MVT supination torque.

Participants were asked to displace the cursor to reach the target and to maintain the cursor within the target sphere, whose radius exceeded that of the cursor by 4% MVFT, for 20 s (holding phase). Targets were displayed in random order and breaks of 40 s were inserted between trials to avoid fatigue. Bipolar EMGs and force data collected during the holding phase of the Baseline block were used to estimate a subject-specific matrix that approximates the mapping of EMG amplitude onto isometric force (see *EMG-to-Force Mapping*) and its null space (30, 35). The maximum amplitude of each rectified and low-pass filtered (second-order Butterworth; 1 Hz cutoff) EMG collected during the same phase was used to normalize EMGs during the Perturbation block. High-density EMGs obtained during the hold phase of all trials of both Baseline and Perturbation blocks were processed for the identification of motor units (MUs). While during the Baseline block, the motion of the cursor was proportional to the exerted force and torque and it was simulated as a single adaptive mass-spring-damper system (MSD), during the Perturbation block it was simulated as two MSDs in series (see Fig. 2*C*), as described in detail by Borzelli et al. (12). Briefly, the force generated by the subject was applied on the first MSD while a simulated sinusoidal force, applied to the second MSD, perturbed the motion of the cursor. The stiffness of the second MSD (k) was modulated in real-time according to the norm of the projection of the muscle activation vector component along the null space of the EMG-to-force matrix ($||\boldsymbol{n}||$), through a logistic function:

$$k(\boldsymbol{n}) = \frac{k_{\max}}{e^{-r_k(||\boldsymbol{n}||-||\boldsymbol{n}_0||)} + 1}, \quad (1)$$

where $k_{\max} = 9{,}500\ \mathrm{Nm}^{-2}$ is the spring constant, $||\boldsymbol{n}_0||$ is set to 2.5 times the minimum norm of the mean null space $||\boldsymbol{n}_{\min}||$, collected during the holding phase of the Baseline block, and it is defined such that $k(\boldsymbol{n}) = \frac{k_{\max}}{2}$, r_k is a variation rate parameter calculated as: $r_k = -\log\left(\frac{{}^{k_{\max}}/_{y_0}-1}{x_0-1}\right)$, and $(x_0, y_0) = \left(||\boldsymbol{n}_{\min}||, 500\ \mathrm{Nm}^{-2}\right)$. Parameters were selected to limit the oscillation of the cursor during the rest phase and assure an adequate reduction of the oscillations during a voluntary cocontraction of muscles, thus guaranteeing that cocontraction exerted by participants effectively modulates the stiffness of the virtual end-effector (12, 36). Therefore, during the Perturbation block, participants could reduce the oscillation of the cursor by cocontracting shoulder and elbow muscles, without affecting the generated end point force required to reach the target. Despite we did not perform any direct measurement on the actual modulation of the arm stiffness, a linear relation between the virtual stiffness and the major axis of the stiffness ellipse was previously demonstrated (30). Moreover, the good level of performance before practice, as demonstrated in previous studies that implemented the virtual stiffness approach (12, 36), suggested that the motor coordination required to reduce the cursor oscillation was not a completely new skill, and likely related to the voluntary cocontraction used to modulate arm stiffness.

Experiment control, data acquisition (force, torque, and bipolar EMG), and data analysis were performed with custom-written software in MATLAB (MathWorks Inc., Natick, MA) and Java.

High-Density Surface Electromyography

Surface EMGs of both heads of biceps brachii (BB) and the lateral head of triceps brachii (TB, see Fig. 2*D*) of each participant were recorded with two arrays, each with 8 × 8 electrodes (3 mm diameter, 10 mm interelectrode distance; HD10MM0808; OT Bioelettronica, Turin, Italy). Participants had their skin cleansed with abrasive paste and the arrays were centered between the proximal and distal tendons of the muscles, with rows visually aligned roughly parallel to the muscle fibers. The array on the BB was placed such that the junction between the long and short heads, identified by palpation, was located between columns 4 and 5. The TB array covered the muscle belly, identified by palpation, and the columns were roughly parallel to the muscle fibers, as indicated by recommendations from SENIAM (37) and Kendall et al. (38). Monopolar EMGs, referenced to the wrist, were amplified and recorded (2,048 Hz sampling rate) using a 16-bit A/D converter (Quattrocento multi-channel amplifier; OT Bioelettronica, Turin, Italy).

Bipolar Surface Electromyography

Bipolar, surface EMGs were recorded from 11 muscles crossing the shoulder and elbow joints: brachioradialis, biceps brachii, pectoralis major, anterior deltoid, middle deltoid, posterior deltoid, triceps brachii long head, infraspinatus, teres major, latissimus dorsi, and middle trapezius. Participants' skin was cleaned with alcohol and electrodes were placed based on recommendations from SENIAM (37) and by palpation to locate the muscle belly and visually orienting the pair of electrodes along the expected direction of fibers. The single bipolar electrode on BB, which was required for the real-time estimation of the null space component of the muscle activation (see *Experimental Design*), was placed just distally to the high-density grid and aligned parallel to the BB long head longitudinal axis. Owing to the skin-parallel fibered architecture of BB, bipolar electrodes placed just distally to the grid would be expected to provide EMGs as representative as those detected more proximally and not in proximity to the muscle innervation zone (39). Bipolar signals were acquired at 1,000 Hz with active wireless bipolar surface electrodes (Trigno System, Delsys Inc., Natick, MA), bandpass filtered (20–450 Hz), and amplified with a 1,000 gain. High-density and bipolar EMGs and force data were recorded by two different data acquisition systems and were synchronized offline using a trigger signal delivered at the beginning of each acquisition by one system and recorded by the second system.

EMG-to-Force Mapping

Isometric generation of submaximal force and torque allowed to use a linear approximation of the relation between EMG amplitude and force and torque:

$$\boldsymbol{f} = H\boldsymbol{m}, \quad (2)$$

where $\boldsymbol{f}$ is a tridimensional vector composed by two components of force exerted along the horizontal plane and one component of supination torque, $\boldsymbol{m}$ is a 11-dimesional muscle activation vector, and H is an EMG-to-force matrix that maps muscles activation onto force. The matrix H was estimated using multiple linear regressions of each low-pass filtered (second-order Butterworth; 1 Hz cutoff) force component, on the rectified, low-pass filtered (second-order Butterworth; 1 Hz cutoff) and normalized to the MVFT bipolar EMGs recorded during the holding phase of the Baseline block (40, 41). The matrix H was also used to compute a null space matrix N, i.e., an orthonormal basis spanning the subspace of vectors $\boldsymbol{n}$ that are mapped by the H matrix onto the null force vector:

$$0 = H\boldsymbol{n}. \quad (3)$$

Motor Unit Decomposition

Monopolar, high-density EMGs were filtered (second-order zero-lag Butterworth, 15–350 Hz) and decomposed through an automatic and validated algorithm (19–21), separately for each 20-s holding phase. After decomposition, the firing instants of identified MUs were visually edited to manually exclude the spikes with lower quality from the calculation of the separation filter (42). The accuracy of the decomposed units was assessed through the pulse-to-noise ratio (PNR) (43), which measures the mean square error between the true discharge pattern of each identified unit and its estimation. Only motor units with a PNR $>$ 30 dB, which assured a sensitivity $>$90% and a false-alarm rate $<$2% (43), were retained. The firing instants of the identified MUs were used to trigger and average single differential EMGs over 30-ms epochs, to provide the action potential of each MN that underwent an additional visual analysis aimed at detecting spurious units (40, 44, 45). Moreover, only units whose action potential was clearly represented on a single muscle were retained, to avoid misleading results due to cross talk. Finally, only units whose firing rates were stable over the entire contraction (pauses shorter than 500 ms) and whose action potential propagation (i.e., the shifting in time of the action potential peak, identified on channels placed along the fiber direction, proportionally to its spatial distance from the innervation zone) could be appreciated, were used in analysis. The activity of each MU was expressed as a binary spike train in which each time sample (2,048 Hz sampling frequency) was assigned either a value of 1 if it marked the beginning of an action potential (identified by the algorithm for MU decomposition) or a value of 0 otherwise. Trials in which fewer than three motor units were decomposed were excluded from the following analyses. In the following analysis, we replicated, on the BB and the TB muscles, the approach that Laine et al. (23) proposed to determine the cross-muscle coherence, the total within-muscle coherence, and the residual within-muscle coherence on the vastus medialis and vastus lateralis muscles.

Cross-Muscle Analysis

In the cross-muscle analysis (see Fig. 3), we calculated the synchronous modulation of the spike trains of MUs identified in the two antagonist muscles during each trial, in both time and frequency domains.

The synchronization in the time domain was calculated through the cross-correlogram, which detects the occurrence of a synchronization between the firings of MNs (32, 42, 46, 47). The cumulative spike trains, calculated from each muscle during each trial, was convoluted with a 400-ms Hanning window (48), which limited the effect of the nonlinear relationship between the synaptic input and the output signal (49), to obtain the smoothed discharge rates. Moreover, a high-pass filter, with cut-off frequency of 0.75 Hz, was applied to remove trends and offsets (48, 50). Then, the filtered cumulative spike trains underwent the cross-correlation analysis, within a time lag of $-$100 to $+$100 ms and 5-ms overlap (22), to determine the common input level between MNs identified on BB and TB during each trial.

The spectral properties of the modulation of the firing rates of motor unit pairs were tested using coherence analysis. Coherence (51) is a frequency domain extension of Pearson's correlation, estimating the linear correlation between the two signals at any given frequency. The coherence analysis was already performed between the overall EMG signals collected from different muscles. However, the coherence analysis has been widely used to calculate the synchronous modulation of pools of MNs identified through needle EMG (18, 52, 53) or high density sEMG (23, 49, 54). We calculated the coherence between the spike trains of all pairs of MUs identified in the two antagonist muscles during each trial. As in the study by Laine et al. (23), all unique pairs of spike trains, identified on the BB and on the TB muscles during a trial, were concatenated into two long trains, which were then subjected to coherence analysis. Each MU train of spikes (here called i and j) was divided into segments of 3-s length. Then, the fast Fourier transform (FFT) ($I_u(f)$ and $J_u(f)$ respectively, which were functions of the frequency f) was calculated over each segment u, considering a 0% overlapping and weighted by a rectangular window function. The complex values obtained across the segments at each frequency were used to derive the auto-spectra (ii and jj) and cross-spectra (ij) of i and j spike trains:

$$ii(f) = \sum_{u=1}^{N} I_u(f) \times \mathrm{conj}(I_u(f)) \quad (4)$$

$$jj(f) = \sum_{u=1}^{N} J_u(f) \times \mathrm{conj}(J_u(f)) \quad (5)$$

$$ij(f) = \sum_{u=1}^{N} I_u(f) \times \mathrm{conj}(J_u(f)) \quad (6)$$

where conj() refers to the complex conjugate of $I_u(f)$ and $J_u(f)$ and N is the number of 3-s length segments.

The magnitude squared coherence (typically referred to as "coherence") for each frequency was then calculated as:

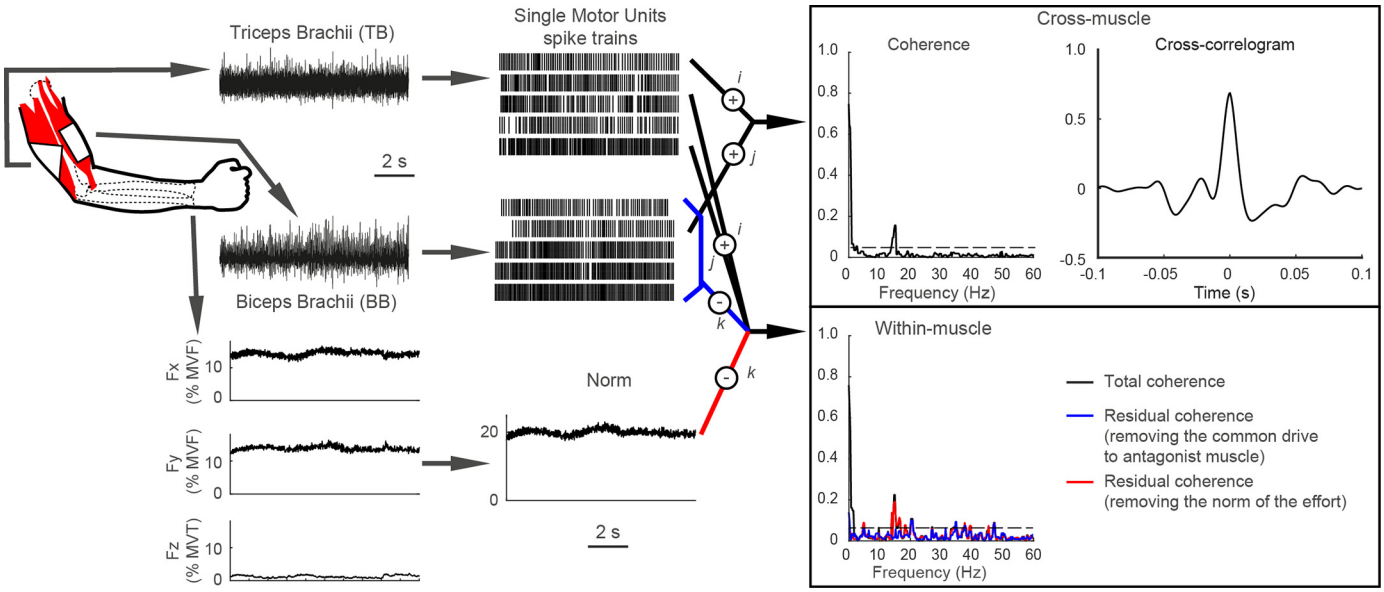

Figure 3. Recordings of high-density electromyogram (EMG) signal and data analysis. High-density EMG signals (64 channels per muscle) were recorded from triceps brachii (TB) and biceps brachii (BB) during submaximal, isometric contractions. These signals were decomposed to reveal the firing pattern of single motor units (MUs). Two approaches were tested. In a cross-muscle analysis (*top right*), we calculated the cross-correlogram and the coherence for paired BB-TB MUs (*i* and *j* signals in *Eqs. 3–6*) identified during a single trial (the example shows data collected during the generation of force to reach target 6 of the Perturbation block, see Fig. 2*B*). In a within-muscle analysis (*bottom right*), we calculated the total coherence between all pairs of MUs from the same TB muscle (*i* and *j* in *Eqs. 3–6*; black trace). We further computed the residual coherence, which represents the within-muscle MU coherence after removing the common neural drive to the antagonist muscle (blue trace) or the effect of force/torque modulation (red trace) contribution (*k* in *Eqs. 7–14*). MVF, maximum voluntary force; MVT, maximum voluntary torque.

$$CohIJ(f) = \left|ij(f)\right|^2 \Big/ (ii(f) \times jj(f)) \quad (7)$$

Each coherence profile was then smoothed in the frequency domain using a three-point running median window.

Coactivation of BB and TB is required both to modulate the elbow stiffness (cocontraction, i.e., without the generation of end point force and torque) or to move the cursor toward a target (e.g., target 2 in Fig. 2*B*), which required the activation of the TB to move the cursor along the horizontal plane, and the activation of BB to generate the supination torque required to move the cursor along the vertical direction. To distinguish these two conditions, the cross-muscle analysis was performed separately on two subsets of target: horizontal targets during the Perturbation block, in which the coactivation was due to the increase in elbow stiffness, and supination targets during the Baseline block, in which no stiffness modulation was required, and therefore coactivation was required to reach the target.

As different spectral characteristics in the firings of the recruited MNs could merely be a consequence of different levels of the HDsEMG activity collected in the two target sets (55, 56), we verified whether BB and TB showed a similar activation during the supination targets of the Baseline block and the Horizontal targets of the Perturbed blocks. We calculated the average rectified value and the power spectrum for the signals collected from each HDsEMG channel of TB and BB, during each trial, and the maximum across channels was retained. ANOVAs were then implemented to test the effects of the block and the participant.

The Matlab code implemented to perform the coherence analyses and the coherence analyses after excluding a third signal, together with exemplificative data, is given in the Supplemental Material (see https://doi.org/10.5281/zenodo.10951228).

Within-Muscle Analysis

In the within-muscle analysis, we isolated the neural drive to each muscle from the contribution of any common drive shared between muscles and responsible for the modulation of force and torque. More specifically, as proposed by Laine et al. (23), we used *Eqs. 3–6* to compute the total coherence, with I_u and J_u corresponding to the FFT of all concatenated unique pairs of spike trains identified on the same muscle during each trial. The residual coherence is an estimation of the synchronous modulation of the firing rate of two MUs (*i* and *j*) in the same muscle, after removing the component that is synchronous to a third reference signal (*k*). In this analysis, *k* represented the common neural activity of all units of the antagonist muscle, calculated as the summation of all individual MU spike trains recorded from the antagonist muscle (23, 57), or as the norm of the force and torque, normalized to the MVFT (Fig. 3).

We first derived the auto-spectra *kk*, which is a function of the frequency *f*, for the reference signal *k* as described for *i* and *j* earlier (3–4). Then, the cross-spectra of signal *k* with signals *i* and *j* were calculated as follows:

$$ik(f) = \sum_{u=1}^{N} I_u(f) \times \mathrm{conj}(K_u(f)) \quad (8)$$

$$ki(f) = \sum_{u=1}^{N} K_u(f) \times \mathrm{conj}(I_u(f)) \quad (9)$$

$$jk(f) = \sum_{u=1}^{N} J_u(f) \times \text{conj}(K_u(f)) \quad (10)$$

$$kj(f) = \sum_{u=1}^{N} K_u(f) \times \text{conj}(J_u(f)) \quad (11)$$

And the cross-spectra and auto-spectra between i and j not due to k signal were calculated as follows:

$$ii\_k(f) = jj(f) - {}^{(jk(f)\times kj(f))}/_{kk(f)} \quad (12)$$

$$jj\_k(f) = ii(f) - {}^{(ik(f)\times ki(f))}/_{kk(f)} \quad (13)$$

$$ij\_k(f) = ij(f) - {}^{(ik(f)\times kj(f))}/_{kk(f)} \quad (14)$$

Therefore, the residual coherence between i and j after removing the component synchronized with k was calculated as follows:

$$CohIJ\_k(f) = {}^{\left|ij\_k(f)\right|^2}/_{(ii\_k(f)\times jj\_k(f))} \quad (15)$$

Residual coherence was computed and then averaged for all pairs of units (i and j) in each of the two muscles, one at a time, with the sum of the spike trains of the other muscle or the norm of the force and torque (normalized to the MVFT), providing the reference signal (k). Total coherence, residual coherence after removing the component synchronous to the common drive to the antagonist muscle, and residual coherence after removing the component synchronous to the norm of the force and torque were computed separately for each participant and trial of the Perturbation block.

Task-Based Separation of Motor Units

Different frequency bands were defined according to functional properties. These bands were the δ band, commonly below 5 Hz (54), the α band, in the [5–12] Hz range (58), the low-β band, below 25 Hz (59), and the high-β band, up to 35 Hz (22). In this study, we opted to separate the low-β ([12–25] Hz) from the high-β ([25–35] Hz) frequency bands as different corticomuscular coherence levels were detected in these two bands in participants who exerted low static forces (59). Moreover, we set the lower threshold of the δ band to 1 Hz to exclude the effect of the mean firing rate of the investigated MNs.

A significant total coherence and a significant residual coherence in the same frequency band in a MU pair, identified during the same trial on the same muscle, indicates that the two units synchronously modulate their firing pattern at that frequency without sharing a common input with the reference signal. In contrast, a significant total coherence without a significant residual coherence indicates that the two units share the same input with the reference signal. Therefore, we defined two criteria, which defined whether a pair of units was recruited to generate force and torque or to modulate the level of cocontraction. A pair of MUs was considered to be driven by a common synaptic input for force generation if they showed a significant total coherence but did not show a significant residual coherence when excluding the component synchronized with the force and torque in a frequency band. Similarly, a pair of MUs was considered to be driven by a common synaptic input for cocontraction modulation if they showed a significant total coherence but did not show a significant residual coherence when excluding the component synchronized with the common drive to the antagonist muscle in the same band.

Therefore, according to total and residual coherence, we could identify three subsets of MUs. One subset was recruited only to generate force, as these MUs satisfied, in all pairings with other units extracted from the same muscle during the same trial, only the criteria for force generation. A second subset was recruited only to modulate cocontraction, as these MUs satisfied only the criteria for cocontraction modulation. A third subset of MUs was recruited both to modulate cocontraction and generate force, as these MUs satisfied both the criteria for force generation and for cocontraction modulation. This separation of MUs into subsets was defined within each frequency band, and therefore, different subsets were defined for each of the four selected frequency bands (δ, α, low-β, and high-β bands). Such assignment of a MU to a subset is strict, because the violation of the criterion even at a single-frequency bin during a single pairing would exclude that MU from the selected subset. For this analysis, each MU train of spikes was divided into segments of 1-s length.

Finally, we calculated the total coherence among all pairs of MUs, identified on the same trial, within these subsets of MUs to determine the frequency band of their common neural input.

Statistics

Based on the null hypothesis that no coherence exists at a given frequency, we defined a 95% confidence level (CL) through surrogate data analyses. Surrogate spike trains were generated for each MN by bootstrapping, i.e., randomly shuffling, the interspike interval (48). This random spike train preserved the same number of spikes and the same average discharge rate of the original one. Moreover, a surrogate force profile was generated by first calculating the Fourier transform, then randomly shuffling the phase components, and finally calculating the inverse Fourier transform (60). This procedure uncorrelated the signal while preserving its power spectrum. The analysis implemented to calculate the cross-correlogram and the within-muscle and cross-muscle coherence were replicated with the surrogate cumulative spike train, calculated by summing the surrogate binary spike trains, and the surrogate force profile. The CL was assessed as the 95th percentile over 100 repetitions.

To assess whether a significant coherence at a specific frequency bin occurred in a significant number of trials or MN pairs, a binomial test was implemented, and a $P < 0.05$ threshold was set. The test provided a conservative evaluation of the relevant frequency content of neural drive within- and between muscles (23).

RESULTS

Motor Unit Decomposition

After exclusion of MUs with a nonphysiological action potential or firing rate, and trials in which no MUs were

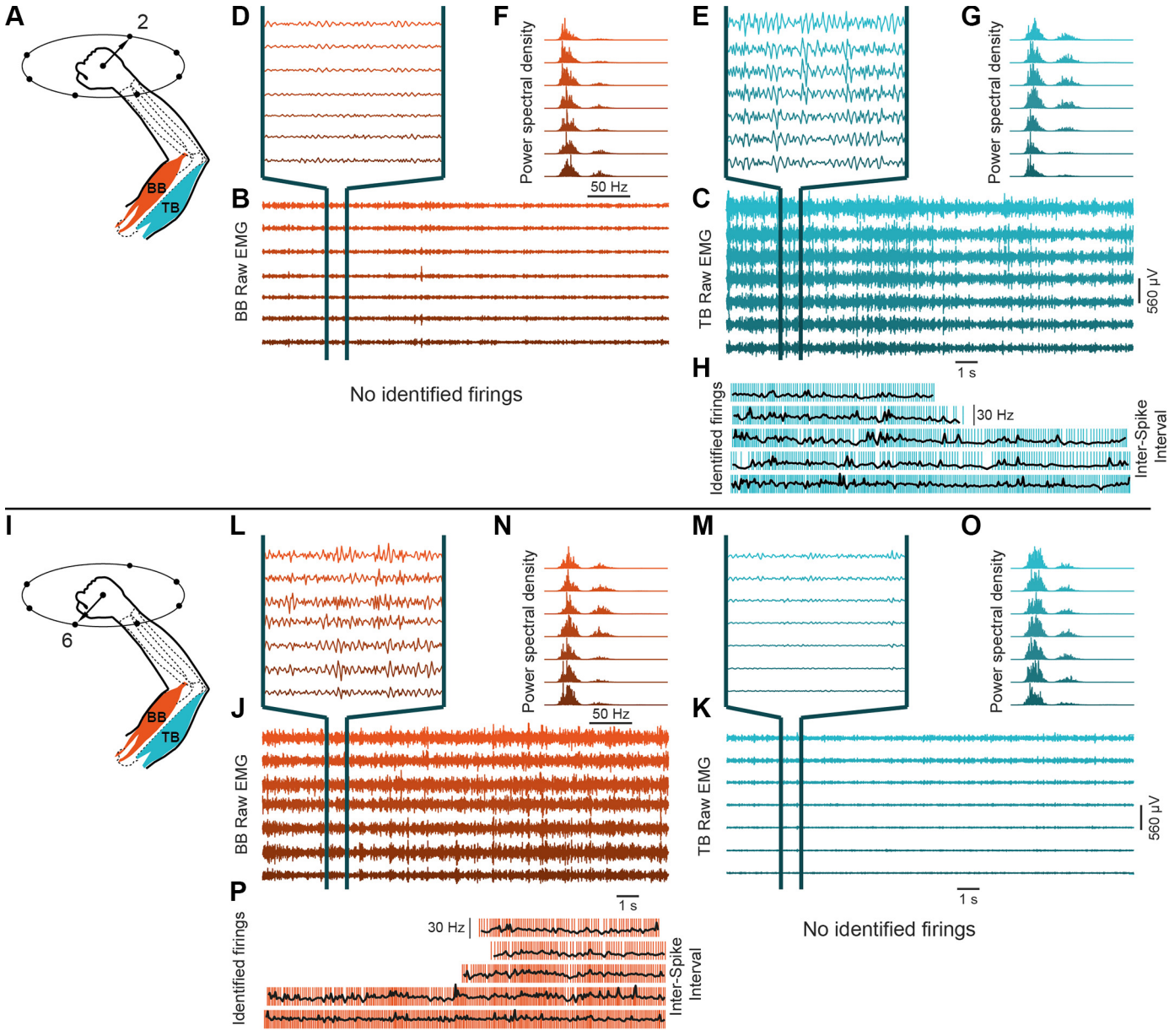

Figure 4. Example of the electromyogram (EMG) signal acquired by a column of channels collecting the activity of biceps brachii (BB) and another collecting the activity of triceps brachii (TB) and the identified firings. The data were collected during the generation of force along two opposite directions on the horizontal plane: one, along target 2 (see Fig. 2*B*), required a torque of elbow extension (*A*) whereas the other, along target 6, required a torque of elbow flexion (*I*). The raw (unprocessed) EMG activity collected from the BB (*B* and *J*, with a portion of the signals expanded respectively in *D* and *L*) and from the TB (*C* and *K*, expanded in *E* and *M*) shows a typical power spectral density (*F*, *G*, *N*, and *O*). The firings of the identified motor units (MUs) on the TB during the generation of a force along target 2 are reported in *H*, whereas the firings of the identified MUs on the BB during the generation of a force along target 6 are reported in *P*. *H* and *P* also showed the interspike interval (black line) of each identified MU. Consistently with the observation that BB was inactive during the generation of a force along target 2 and TB was inactive during the generation of a force along target 6, no MUs were identified.

identified on the BB or on the TB (Fig. 4), a total of 1,705 MUs were retained for the analysis (Table 1). Different numbers of MUs were extracted from data collected during different trials because their activation was modulated according to the end point force. The maximum number of units identified on the BB during Baseline block or the Perturbed block was 5 (4) and 5.5 (5.5) respectively [median (interquartile range)], and the maximum number of units identified on the TB during Baseline block or the Perturbed block was 7 (4) and 9.5 (2.5) respectively. In line with the literature (61), the BB median discharge rate ranged between 8.2 and 35.8 spikes/s and the TB median discharge rate ranged between 8.5 and 29.6 spike/s, showing, on average, 13.6 ± 1.4 (means ± SD) spikes/s for the BB and 12.7 ± 1.6 spikes/s for the TB during the baseline block, and were 14.2 ± 1.4 spikes/s for the BB and 14.2 ± 2.3 spikes/s for the TB during the perturbed block. In Fig. 4, examples of data collected from BB and TB during the exertion of two force target of the baseline block, and the related MUs extracted from data, are shown. In Fig. 4, examples of data collected

Table 1. *Number of MUs retained for the analysis*

Block	BB		TB		Total	
	n	Median (IQR)	*n*	Median (IQR)	*n*	Median (IQR)
Baseline	357	44 (26)	320	33 (31.5)	677	83 (41.5)
Perturbation	598	76.5 (14.5)	430	46.5 (47)	1,028	121.5 (63)
Total	955	122.5 (30)	750	80 (76)	1,705	209 (99.5)

Median and interquartile range (IQR) across subjects. BB, biceps brachii; MUs, motor units; TB, triceps brachii.

from BB and TB during the exertion of two force target of the Baseline block, and the related MUs extracted from the data, are shown.

As the EMG signal represents the sum of the action potentials of all the active MNs, its power spectrum (an example is shown in Fig. 4) does not match the power spectrum of the firings of the extracted MNs. However, the EMG signal is influenced by the electrical properties of the muscle fibers (62, 63), and therefore the MN firings represents a better description of the neural input that drives muscles.

Cross-Muscle Analysis

First, we assessed whether discrepancies in the synchronization among MNs recruited during a stiffness modulation task or a force/torque generation task could merely be ascribed to different activations of the muscle, which may imply a different number of the recruited MNs (56) and their firing rates (55). However, an ANOVA did not show any significant effect neither on the EMG amplitude nor in the power spectral density of horizontal targets during Perturbed block or supination targets during Baseline block, neither in BB ($P = 0.42$ and $P = 0.71$, respectively for EMG amplitude and power spectral density) nor in TB ($P = 0.35$ and $P = 0.81$, respectively for EMG amplitude and power spectral density).

A total of 40 trials of the Perturbation block [with a median (interquartile range) over participants of 5 (4)], and 42 trials of Baseline block [6 (4)], respected the conditions to be included in the cross-muscle analyses.

Figure 5, *A* and *B* depict the cross-correlogram between the cumulative spike trains of MUs identified during the generation of force to reach the horizontal targets of the Perturbation block (Fig. 5*A*) or the supination targets of the Baseline block (Fig. 5*B*). Values greater than the marked confidence level (dashed line) indicated that the cross-correlation was substantially higher than expected by chance. Remarkably, the cross-correlogram performed only on the trials collected during voluntary modulation of cocontraction (Fig. 5*A*) showed a significant peak of correlation at a lag close to 0 s, commonly ascribed to a common synaptic input (18, 32), suggesting a synchronization between the MNs of the two muscles when recruited to modulate the cocontraction. In contrast, despite the cross-correlogram calculated from the trials that required the coactivation of BB and TB to generate force also showed a peak at a lag close to 0 s (Fig. 5*B*), its value was below the chance threshold.

Figure 5, *C* and *D* depicts the percentage of trials that showed significant BB-TB coherence (95% confidence level) identified during the generation of force to reach

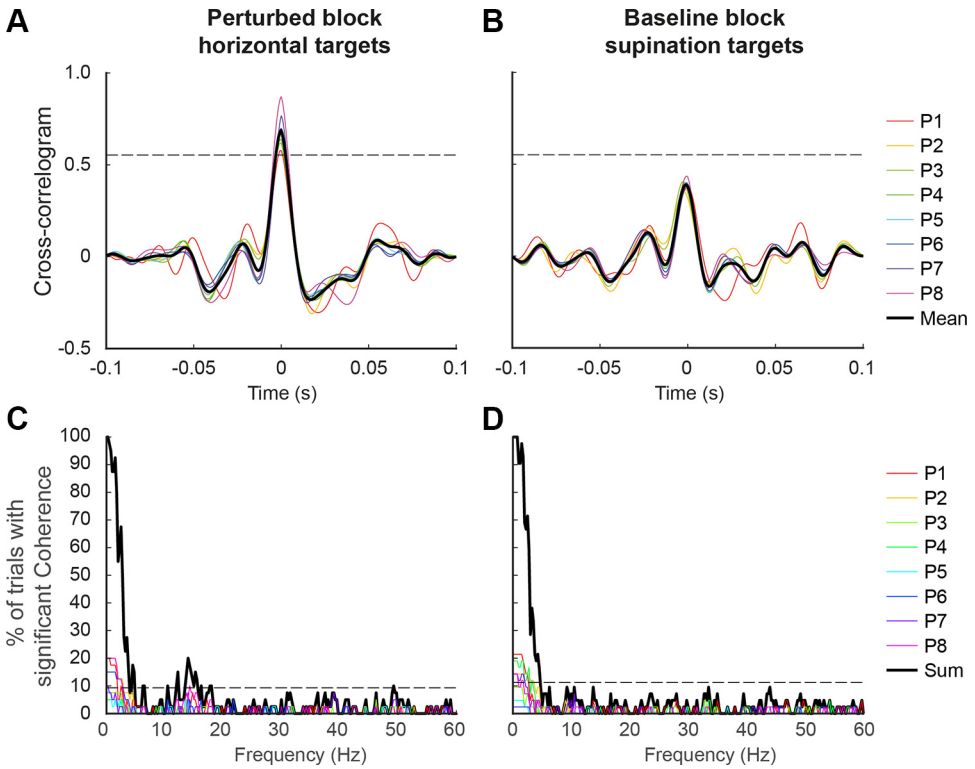

Figure 5. Cross-muscle analysis: cross-correlogram and percentage of the pairs of motor units (MUs), identified on antagonist muscles, showing a significant coherence. The cross-correlogram was calculated on the cumulative spike trains of the MUs identified, during the same trial, on the antagonist muscles. Trials that required reaching horizontal targets of the Perturbation block (*A*) and the supination targets of the Baseline block (*B*) were separated. The coherence analysis was performed on all pairs of MUs, identified on the biceps brachii (BB) and the triceps brachii (TB) muscles during the horizontal targets of the Perturbation block (*C*) and the supination targets of the Baseline block (*D*). The dashed horizontal line indicates the highest proportion that could have been observed simply by chance (95% confidence level). Subject-specific cross-correlogram values or fraction of significant coherence, are reported with different colors. Black solid lines indicated the cross correlogram, averaged among participants (*A* and *B*) or the sum of all the trials showing a significant coherence (*C* and *D*).

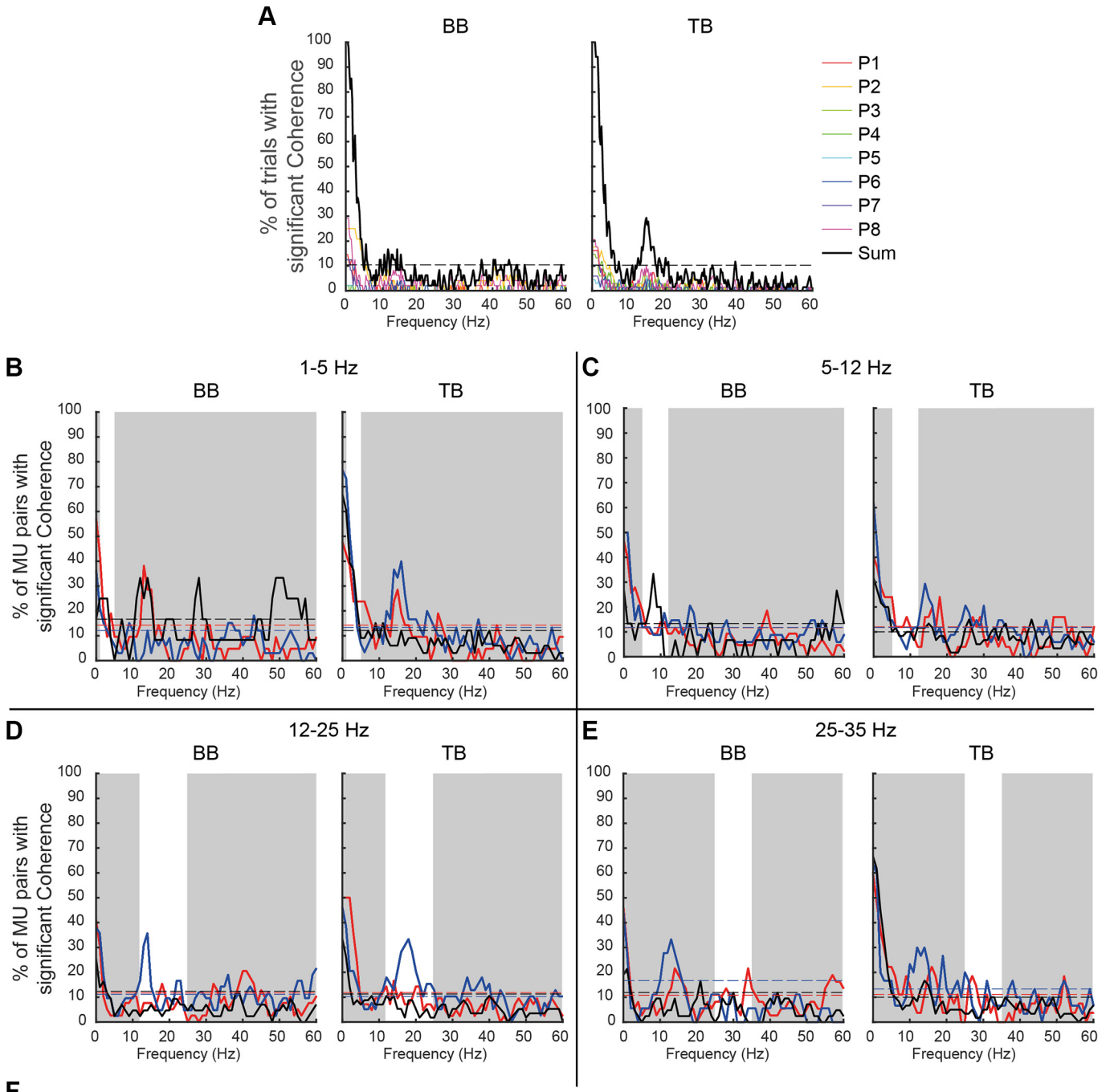

F

	1-5 Hz		5-12 Hz		12-25 Hz		25-35 Hz	
	BB	TB	BB	TB	BB	TB	BB	TB
MUs involved in the modulation of stiffness	19%(44)	13%(42)	21%(49)	20%(65)	26%(60)	22%(71)	14%(32)	18%(58)
MUs involved in the generation of force/torque	15%(35)	11%(36)	15%(35)	15%(49)	22%(51)	20%(65)	21%(49)	17%(55)
MUs involved in the generation of both stiffness and force/torque	16%(37)	18%(58)	22%(51)	22%(71)	24%(56)	22%(71)	21%(49)	25%(81)

the horizontal targets of the Perturbation block (Fig. 5*C*) or the horizontal targets of the supination targets of the Baseline block (Fig. 5*D*). Fractions greater than the marked confidence level (dashed line) indicated that significant coherence occurred in a substantially higher number of trials than expected by chance. The cross-muscle coherence analysis performed on both the target sets identified a [0–5] Hz component of the synchronous modulation between the MNs identified in the muscles. Although the significant coherence close to 0 Hz reflected data with nonzero mean, the significant coherence at higher frequencies up to 5 Hz is responsible for the generation of the muscle tension (64). Remarkably, another significant peak was identified between 12 and 20 Hz only when participants were required to exert a force and to increase BB-TB cocontraction (Fig. 5*C*). This second peak in the coherence between the discharge trains of the MNs located on antagonist muscles, together with the significant peak in the cross-correlogram, identified only during the tasks requiring cocontraction for stiffness modulation (horizontal targets in the Perturbation block) revealed the existence of shared inputs to these muscles and supported the hypothesis of a specific input for the modulation of cocontraction that is independent from the input for the generation of force.

Task-Based Separation of Motor Units

Although the cross-muscle analysis investigated the coherence between pairs of units identified on antagonist muscles, the within-muscle analysis investigated the coherence between units identified on the same muscle, considering all frequency components (total coherence) or excluding the components synchronized with the common drive to the antagonist muscle or with the exerted force and torque (residual coherence).

A total of 48 trials of the Perturbation block [with a median (interquartile range) over participants of 6 (8.5)] for BB and a total of 68 trials [8.5 (6)] for TB were included in the within-muscle coherence. Figure 6*A* depicts the percentage of MU pairs, identified on all trials of the Perturbation block, that showed a significant total within-muscle coherence, for TB (Fig. 6*A*) and BB (Fig. 6*B*). Besides the significant peak below 10 Hz, whose role was to effectively modulate the force generated by the muscle (57), both BB and TB showed several frequency bins with a significant percentage (i.e., above the dashed horizontal line) of pairs of MUs with total coherence in the 12–22 Hz band.

We then used the total and residual within-muscle coherence of to identify three subsets of MUs in each muscle. The analysis was performed on 232 [median (interquartile range) across participants: 20.5 (43)] and 325 [40.5 (32)] MNs, respectively identified in BB and TB. The selected frequency bands were identified as functionally relevant as the δ ([1–5] Hz, Fig. 6*B*), α ([5–12] Hz, Fig. 6*C*), low-β ([12–25] Hz, Fig. 6*D*), and high-β ([25–35] Hz, Fig. 6*E*) bands. The percentages of MNs that were identified to be selectively recruited to modulate the cocontraction or to generate force are reported in Fig. 6*F*. The lower boundary of the δ band was set to 1 Hz instead of 0 Hz to overcome the effect of the discrepancy of the mean firing rate on the low frequency. As the MN separation was performed on a specific frequency interval, within-set coherence was also analyzed in the same interval (visually reported in Fig. 6, *B–E*).

The total within-set coherence among these subsets of units revealed peaks at different frequency bands. Although all the MU sets identified both on the TB and BB showed a significant coherence peak below 5 Hz (Fig. 6*B*), in the [5–12] Hz band (Fig. 5*C*) only pairs of BB MNs involved in both tasks (black line) and pairs of TB MNs involved in force generation task (red line) showed a significant coherence, confirming the role of the α band in the force generation (57). Surprisingly, a striking fraction of pairs of MNs, involved in the modulation of stiffness (blue line), showed a significant coherence in the [12–25] Hz band both in BB and TB (Fig. 5*D*). The MNs that were separated in the three sets, and that were investigated to detect the coherence peak in the [12–25] Hz band, represented respectively the 72% and the 64% of the MNs identified on the BB and on the TB (Fig. 6*F*). Finally, in the [25–35] Hz band, MNs involved in force generation showed some peaks, slightly above the confidence level, both in the TB and the BB, whereas MNs involved in stiffness modulation, showed some significant peaks, slightly above the confidence level, on the only TB (Fig. 5*E*).

DISCUSSION

We investigated the control of a pair of muscles at the motor neuron level and the different neural pathways responsible for the modulation of the limb stiffness and for the generation of force. Several studies had suggested that antagonist muscles coactivated to modulate stiffness (25, 26), similarly to synergistic muscles coactivated to generate force (23, 25, 28, 29), are controlled by a common synaptic input. However, the spectral features that differentiate the inputs underlying these two functionally different tasks have not been investigated. Therefore, we designed a novel experimental paradigm that required a participant to coactivate

Figure 6. Total within-muscle motor unit (MU) coherence and common input to MUs driving the generation of force and torque or the modulation of stiffness. *Top*: the percentage of the pair of MUs, identified on the biceps brachii (BB) (*left portion of A*) or on the triceps brachii (TB) (*right portion of A*), that showed a significant total within-muscle coherence. Subject-specific values were reported with different colors, while their sum was reported with a solid black line. *B–E:* the total within-muscle coherence separately calculated among the subset of MUs selectively recruited to modulate cocontraction or generate force and torque in TB and BB. The fraction of pairs that showed a significant coherence is displayed in the figure (blue: MUs selectively recruited to modulate cocontraction; red MUs selectively recruited to generate force and torque, black: MUs recruited both to modulate cocontraction and force/torque). The separation among sets was performed according to different physiologically relevant frequency bands: δ band ([1–5] Hz, *B*), α band ([5–12] Hz, *C*), low-β band ([12–25] Hz, *D*), high-β band ([25–35] Hz, *E*). The band used to separate MUs on the three different sets showed a white background, whereas the excluded band show a gray background. In *A–E*, the horizontal dashed lines represent the threshold for significance, i.e., the higher value of the 95% confidence interval of the percentage of MU pairs that may show significant coherence by chance. In *B–E*, the difference between the confidence levels is due to the different numbers of pairs of MUs involved in the modulation of cocontraction or in the generation of force and torque. The number of motor neurons (MNs) (in parentheses) and its fraction of the total number (i.e., 232 and 325 respectively for BB and TB), involved in this analysis, which composed the different sets, was reported, for each frequency band, in *F*.

the same muscle pair to perform two functionally different tasks: generation of force and modulation of stiffness. The spike trains of MUs were identified by decomposing the high-density EMG signals collected from the BB and the TB muscles by means of an established algorithm (19–21), whereas the common drive to motor units of two antagonist muscles was identified by means of coherence analysis (29). The generation of different isometric torques may lead to a shifting of the innervation zone (65, 66), with the consequent alteration in the action potentials, recorded by the HDsEMG grid. Therefore, as our study did not require the tracking of MNs across different conditions, we preferred to investigate pools of MNs extracted separately from different trials and blocks, in line with previous studies (23). Intriguingly, a cross-muscle analysis identified a significant synchronization, measured through the cross-correlogram, only when the muscle pair was recruited to modulate the stiffness and not to generate the force. On the other hand, cross-muscle coherence detected a wide frequency band (between 15 and 20 Hz) in a significantly larger portion of trials than expected by chance only when BB and TB were coactivated to modulate cocontraction. This result, therefore, suggests that the MN pools identified for different muscles share separate synaptic inputs, whose synchronization and spectral characteristics differ according to the functional task.

A within-muscle analysis identified subsets of MUs that were selectively recruited either to generate force, or to modulate cocontraction, or for both tasks. Although a low-frequency peak (<5 Hz) was identified between all the MN subsets, a peak in the α band (5–12 Hz) was identified only between MNs recruited to modulate force or for both tasks. Strikingly, a wide peak in the low-β band (12–25 Hz) was detected only within MNs recruited to modulate stiffness. This band is particularly relevant as significant corticomuscular coherence has been identified during the exertion of low static forces (59).

The existence of a common input driving the MNs of both agonist or antagonist muscles of the hand has previously been demonstrated (25), but only in different pairs of muscles. Therefore, the results may have been affected by the different properties of the muscles involved in that study, rather than on the characteristics of different synaptic inputs underlying the two tasks. To overcome this issue, in this study, we introduced an experimental protocol that allowed to compare the spectral properties of the common input to a pair of muscles, i.e., BB and TB, which could be coactivated to perform two functionally different tasks, i.e., force generation or stiffness modulation. As BB is both an elbow extensor and a wrist supinator, depending also on the activation of other muscles acting on the same joints, its coactivation with TB may result in an increase of the stiffness or a generation of force, depending on the action exerted by the other active muscles.

Therefore, the protocol presented in this study exploited the redundancy of the musculoskeletal system to discriminate the neural drives underlying the generation of force, which were active when BB and TB cooperated to move a virtual cursor into the "supination target" set during the Baseline block, from those recruited to increase the joint stiffness required to reduce the cursor oscillation induced during the reaching of "horizontal targets" of the Perturbed block. As the same MN pool receives different drives (48, 67–69), beyond those in common between BB and TB, we expect muscle-specific synaptic inputs driving the generation of end point force along the horizontal plane, which may decorrelate the output of the shared input (70). Therefore, the target set was defined to require a modulation of the muscle-specific drive across trials, through the generation of force along different horizontal directions, which would reduce its contribution to the muscle's drive, while demanding a constant shared input. In other words, we defined targets that could be reached with a constant supination torque or a constant stiffness level.

The Neural Origin of the Modulation of Cocontraction

Although voluntary actions may be achieved by the recruitment of Ia inhibitory interneurons, which depresses the activity of spinal motoneurons innervating antagonist muscles (71–75), the coactivation of antagonist muscles requires a pathway that both facilitates the simultaneous activation of the antagonistic muscles and maintains a low di-synaptic reciprocal inhibition of Ia interneurons (76). Two separate descending pathways (77) centrally originated (78) and regulated by the cerebellum (79) might drive motoneurons of antagonistic muscle pairs: one activating the agonist while depressing the antagonist, responsible for torque generation, and the other one coactivating both muscles, responsible for stiffness modulation (80). These pathways appear to originate from two distinct anatomical portions of the premotor cortex (14), and to be regulated by intracortical excitatory connections (13). A recent study (15) demonstrated the existence of spinal interneurons mediating cocontraction of antagonist muscles. However, the paradigm proposed in our study exploited two coactivation tasks, both requiring the inhibition of Ia interneurons, but different in the purpose of the coactivation. Coherence between antagonist muscles during a cocontraction task has already been investigated with surface EMG (80–82). However, the surface EMG signal is influenced by the electrical properties of the muscle fibers (62, 63). In contrast, the coherence among the firing trains of a pool of MNs reflects the synaptic input shared within that MN pool (17). The coherence analysis was widely used to calculate the synchronous modulation of pools of MNs identified through needle EMG (18, 52, 53) or high-density sEMG (23, 49, 54).

The results presented in our study provide new insights on the physiological mechanisms underlying the modulation of stiffness at the MN level. Despite the synchronization between MUs of different muscles has long been established in cats (83) and humans (29), its anatomical origin and physiological role is still unknown. Cocontraction is associated with significant EEG-EMG and EMG-EMG coherence in the β-band among antagonistic muscles, suggesting a direct cortical regulation of both agonist and antagonist muscles (84), although the fluctuations identified during the generation of force are reflected as a coherence peak in the α-band (64, 80). Although the α-band coherence peak that we observed in both coactivation conditions can be related to an input for force generation, the peak in the β-band, observed only during coactivation for stiffness modulation, suggests a cortical origin of the

cocontraction input. However, despite a simulation study has proposed a role of the high-frequency band in force regulation (85), the low-pass filtering performed by the muscles (86) makes a direct contribution of the high frequencies to the control of force unlikely (87, 88). Significant high-frequency corticomuscular coherence (31) derives from the rhythmic discharges of the corticospinal neurons projecting to spinal motoneurons (32). Its increase in functional coupling in infants (89) suggests that the β-band component of the descending control signal modulates the spinal activity (90), which in turn control muscles through effective low-frequency common drive (57).

The residual coherence analysis allowed, through a conservative criterion, to identify three subsets of MNs that were selectively recruited to modulate cocontraction, to generate force, or for both tasks. Task-specific motor units have been reported before (40, 91–93), and this study identified a set of units selectively recruited to modulate cocontraction. Although a significant component of the MN sets involved in the force generation or in both tasks were identified in the α band (5–12 Hz), suggesting the functional role of this band in the generation of force, a strong coherence in the low-β band (12–25 Hz), which reflects the corticomuscular coherence in low static force generation tasks (59), was identified between the subset of MNs only involved in the modulation of stiffness. Taken together, our results suggest the existence of a separate synaptic pathway for stiffness modulation, which is cortically originated and projects to a specific pool of motor units.

In this study, we investigated the common drive to BB and TB during the generation of isometric forces and torques along different directions in a single posture. Altering the posture would modify the joint angles, the moment arms of the muscles, and the length of the muscle fibers, and therefore the number of actomyosin cross-bridges that may be formed. Moreover, different joint angles would imply different moment arms of the muscles acting on that joint, which may lead to an altered ratio between the torques that each muscle may generate. So, the same neural input would generate a different joint torque, or, in other word, the same joint torque may require a different synaptic input to be generated, which would alter the firing of the active MNs or would recruit new MNs. How the activities of two muscles can be synchronized at different joint angles remains an open question that should be investigated in further experiments.

Common Input May Reflect Muscle Synergies

Although our study investigated the recruitment of two antagonist muscles, a previous study by Laine et al. (23) investigated the common drive to a pair of synergistic muscles. As the algorithms implemented in this study replicated those proposed by Laine et al., the comparison between the results presented in the two studies may provide an overall view of the synaptic input shared between pairs of muscles coactivated with physiological characteristics and recruited with different purposes. In particular, the coherence that Laine et al. identified between synergistic muscles showed significant peaks at frequency bands that were close to those identified in this study, where however participants were coactivating their muscles to modulate the stiffness, rather than to generate force/torque. Synaptic drives shared by motor neurons of either synergistic or antagonistic muscles, which do not simply reflects the coactivation of multiple muscles, may represents a neural implementation of muscle synergies, whose existence has been supported by the observation of low-dimensionality in the muscle patterns during several tasks (94–100), and recently a synergistic organization has been detected at the MN level too (101). The presence of a corticosynergistic coherence in the β band (102), would suggest that the β coherence peak that we identified only during coactivation for stiffness modulation between pools of MNs of different muscles, may reflect a common synergistic command.

Neurophysiological Basis for Motor Augmentation

Our results provide a physiological basis for the exploitation of cocontraction to control the stiffness of a robotic device (103–106) and for motor augmentation (107–110). Separate neural pathways driving cocontraction may be exploited as an implicit "task null space" (111) to control extra degrees of freedom without affecting the control of the natural degree of freedom involved in performing a task. Similarly, the β-component of the common drive could be volitionally modulated to control a cursor in real-time (112). The feasibility of the use of cocontraction in motor augmentation has been recently demonstrated during an isometric multi-muscle force generation task (36). Moreover, the proposed approach may be transferred to patients with neuromuscular disorders, such as stroke (113), dystonia (114), or Parkinson disease (115), to characterize pathological features in the synaptic input to multiple coactive muscles that differs from healthy subjects.

Conclusions

Overall, our study has expanded the current understanding of the control of multiple muscles by demonstrating, for the first time, specific spectral characteristics in the coherence between the synaptic inputs to the same muscle pair underlying functionally different tasks.

DATA AVAILABILITY

Source data for this study are not publicly available due to privacy or ethical restrictions. The source data are available to verified researchers upon request by contacting the corresponding author.

SUPPLEMENTAL DATA

Supplemental Material: https://doi.org/10.5281/zenodo.10951228.

ACKNOWLEDGMENTS

We thank Julien Rossato for support in the diagnostic of the firings of motor units. Preprint is available at https://doi.org/10.1101/2022.08.18.504426.

Present address of A. d'Avella: Dept. of Biology, University of Rome Tor Vergata, Rome, Italy.

GRANTS

This work was supported by the Italian University Ministry PRIN Grant 2015HFWRYY, PRIN Grant 2017CBF8NJ, PRIN Grant

2020EM9A8X, and NRRP Project MNESYS PE00000006; and the European Union Project HARIA, EU Horizon Europe, GA No. 101070292.

DISCLOSURES

No conflicts of interest, financial or otherwise, are declared by the authors.

AUTHOR CONTRIBUTIONS

D.B., T.M.M.V., A.B., M.G., and A.d. conceived and designed research; D.B. performed experiments; D.B. analyzed data; D.B., T.M.M.V., A.B., M.G., F.L., and A.d. interpreted results of experiments; D.B., T.M.M.V., and A.d. prepared figures; D.B., T.M.M.V., and A.d. drafted manuscript; D.B., T.M.M.V., A.B., M.G., F.L., and A.d. edited and revised manuscript; D.B., T.M.M.V., A.B., M.G., F.L., and A.d. approved final version of manuscript.

REFERENCES

1. **Bernstein NA.** *The Co-ordination and Regulation of Movements* (1st English ed.). Oxford, UK: Pergamon Press, 1967.
2. **Hogan N.** Adaptive control of mechanical impedance by coactivation of antagonist muscles. *IEEE Trans Automat Contr* 29: 681–690, 1984. doi:10.1109/TAC.1984.1103644.
3. **Milner TE.** Adaptation to destabilizing dynamics by means of muscle cocontraction. *Exp Brain Res* 143: 406–416, 2002. doi:10.1007/s00221-002-1001-4.
4. **De Serres SJ**, **Milner TE.** Wrist muscle activation patterns and stiffness associated with stable and unstable mechanical loads. *Exp Brain Res* 86: 451–458, 1991. doi:10.1007/BF00228972.
5. **Latash M.** Independent control of joint stiffness in the framework of the equilibrium-point hypothesis. *Biol Cybern* 67: 377–384, 1992. doi:10.1007/BF02414893.
6. **Burdet E**, **Osu R**, **Franklin D**, **Milner T**, **Kawato M.** The central nervous system stabilizes unstable dynamics by learning optimal impedance. *Nature* 414: 446–449, 2001. doi:10.1038/35106566.
7. **Lacquaniti F**, **Maioli C.** The role of preparation in tuning anticipatory and reflex responses during catching. *J Neurosci* 9: 134–148, 1989. doi:10.1523/JNEUROSCI.09-01-00134.1989.
8. **Selen LPJ**, **Beek PJ**, **Van Dieën JH.** Impedance is modulated to meet accuracy demands during goal-directed arm movements. *Exp Brain Res* 172: 129–138, 2006. doi:10.1007/s00221-005-0320-7.
9. **Gribble PL**, **Mullin LI**, **Cothros N**, **Mattar A.** Role of cocontraction in arm movement accuracy. *J Neurophysiol* 89: 2396–2405, 2003. doi:10.1152/jn.01020.2002.
10. **Selen LPJ**, **Franklin DW**, **Wolpert DM.** Impedance control reduces instability that arises from motor noise. *J Neurosci* 29: 12606–12616, 2009. doi:10.1523/JNEUROSCI.2826-09.2009.
11. **Haynes EMK**, **Kim C.** Antagonist surface electromyogram decomposition and the case of the missing motor units. *J Neurophysiol* 126: 1943–1947, 2021. doi:10.1152/jn.00435.2021.
12. **Borzelli D**, **Cesqui B**, **Berger DJ**, **Burdet E**, **d'Avella A.** Muscle patterns underlying voluntary modulation of co-contraction. *PLoS One* 13: e0205911, 2018. doi:10.1371/journal.pone.0205911.
13. **Ethier C**, **Brizzi L**, **Giguère D**, **Capaday C.** Corticospinal control of antagonistic muscles in the cat. *Eur J Neurosci* 26: 1632–1641, 2007. doi:10.1111/j.1460-9568.2007.05778.x.
14. **Haruno M**, **Ganesh G**, **Burdet E**, **Kawato M.** Differential neural correlates of reciprocal activation and cocontraction control in dorsal and ventral premotor cortices. *J Neurophysiol* 107: 126–133, 2012. doi:10.1152/JN.00735.2010.
15. **Ronzano R**, **Lancelin C**, **Bhumbra GS**, **Brownstone RM**, **Beato M.** Proximal and distal spinal neurons innervating multiple synergist and antagonist motor pools. *eLife* 10: e70858, 2021. doi:10.7554/ELIFE.70858.
16. **Takagi A**, **Kambara H**, **Koike Y.** Independent control of cocontraction and reciprocal activity during goal-directed reaching in muscle space. *Sci Rep* 10: 22333, 2020. doi:10.1038/s41598-020-79526-1.
17. **Farina D**, **Negro F.** Common synaptic input to motor neurons, motor unit synchronization, and force control. *Exerc Sport Sci Rev* 43: 23–33, 2015. doi:10.1249/JES.0000000000000032.
18. **Farmer SF**, **Bremner FD**, **Halliday DM**, **Rosenberg JR**, **Stephens JA.** The frequency content of common synaptic inputs to motoneurones studied during voluntary isometric contraction in man. *J Physiol* 470: 127–155, 1993. doi:10.1113/jphysiol.1993.sp019851.
19. **Holobar A**, **Zazula D.** Multichannel blind source separation using convolution kernel compensation. *IEEE Trans Signal Process* 55: 4487–4496, 2007. doi:10.1109/TSP.2007.896108.
20. **Holobar A**, **Minetto MA**, **Botter A**, **Negro F**, **Farina D.** Experimental analysis of accuracy in the identification of motor unit spike trains from high-density surface EMG. *IEEE Trans Neural Syst Rehabil Eng* 18: 221–229, 2010. doi:10.1109/TNSRE.2010.2041593.
21. **Holobar A**, **Minetto MA**, **Botter A**, **Farina D.** Identification of motor unit discharge patterns from high-density surface EMG during high contraction levels. In: *5th European Conference of the International Federation for Medical and Biological Engineering*, edited by Jobbágy Á. Berlin, Heidelberg: Springer, 2012, p. 1165–1168.
22. **Del Vecchio A**, **Falla D**, **Felici F**, **Farina D.** The relative strength of common synaptic input to motor neurons is not a determinant of the maximal rate of force development in humans. *J Appl Physiol (1985)* 127: 205–214, 2019. doi:10.1152/japplphysiol.00139.2019.
23. **Laine CM**, **Martinez-Valdes E**, **Falla D**, **Mayer F**, **Farina D.** Motor neuron pools of synergistic thigh muscles share most of their synaptic input. *J Neurosci* 35: 12207–12216, 2015. doi:10.1523/JNEUROSCI.0240-15.2015.
24. **Martinez-Valdes E**, **Laine CM**, **Falla D**, **Mayer F**, **Farina D.** High-density surface electromyography provides reliable estimates of motor unit behavior. *Clin Neurophysiol* 127: 2534–2541, 2016. doi:10.1016/j.clinph.2015.10.065.
25. **Bremner FD**, **Baker JR**, **Stephens JA.** Variation in the degree of synchronization exhibited by motor units lying in different finger muscles in man. *J Physiol* 432: 381–399, 1991. doi:10.1113/jphysiol.1991.sp018390.
26. **De Luca CJ**, **Mambrito B.** Voluntary control of motor units in human antagonist muscles: Coactivation and reciprocal activation. *J Neurophysiol* 58: 525–542, 1987. doi:10.1152/jn.1987.58.3.525.
27. **Nielsen J**, **Kagamihara Y.** Synchronization of human leg motor units during co-contraction in man. *Exp Brain Res* 102: 84–94, 1994. doi:10.1007/BF00232441.
28. **Bremner FD**, **Baker JR**, **Stephens JA.** Correlation between the discharges of motor units recorded from the same and from different finger muscles in man. *J Physiol* 432: 355–380, 1991. doi:10.1113/jphysiol.1991.sp018389.
29. **De Luca CJ**, **Erim Z.** Common drive of motor units in regulation of muscle force. *Trends Neurosci* 17: 299–305, 1994. doi:10.1016/0166-2236(94)90064-7.
30. **Borzelli D**, **Pastorelli S**, **d'Avella A**, **Gastaldi L.** Virtual stiffness: a novel biomechanical approach to estimate limb stiffness of a multi-muscle and multi-joint system. *Sensors* 23: 673, 2023. doi:10.3390/s23020673.
31. **Kristeva-Feige R**, **Fritsch C**, **Timmer J**, **Lücking CH.** Effects of attention and precision of exerted force on beta range EEG-EMG synchronization during a maintained motor contraction task. *Clin Neurophysiol* 113: 124–131, 2002. doi:10.1016/S1388-2457(01)00722-2.
32. **Farmer SF**, **Halliday DM**, **Conway BA**, **Stephens JA**, **Rosenberg JR.** A review of recent applications of cross-correlation methodologies to human motor unit recording. *J Neurosci Methods* 74: 175–187, 1997. doi:10.1016/S0165-0270(97)02248-6.
33. **de Souza LML**, **Cabral HV**, **de Oliveira LF**, **Vieira TM.** Motor units in vastus lateralis and in different vastus medialis regions show different firing properties during low-level, isometric knee extension contraction. *Hum Mov Sci* 58: 307–314, 2018. doi:10.1016/j.humov.2017.12.012.
34. **Laine CM**, **Valero-Cuevas FJ.** Intermuscular coherence reflects functional coordination. *J Neurophysiol* 118: 1775–1783, 2017. doi:10.1152/jn.00204.2017.
35. **Lay D**, **Lay S**, **McDonald J.** *Linear Algebra and Its Applications* (5th ed.). Boston, MA: Pearson, 2014.
36. **Gurgone S**, **Borzelli D**, **Pasquale P**, **de Berger DJ**, **Baldi TL**, **D'Aurizio N**, **Prattichizzo D**, **d'Avella A.** Simultaneous control of natural and extra degrees of freedom by isometric force and electromyographic activity in the muscle-to-force null space. *J Neural Eng* 19: 016004, 2022. doi:10.1088/1741-2552/ac47db.

37. **Hermens HJ**, **Freriks B**, **Merletti R**, **Stegeman D**, **Blok J**, **Rau G**, **Disselhorst-Klug C**, **Hägg G.** *European Recommendations for Surface ElectroMyoGraphy Results of the SENIAM Project*. Enschede, Netherlands: Roessingh Research and Development, 1999.
38. **Kendall F**, **McCreary E**, **Provance P.** Muscles, testing and function. *Med Sci Sports Exerc* 26: 1070, 1994. doi:10.1249/00005768-199408000-00023.
39. **Vieira TM**, **Botter A.** The accurate assessment of muscle excitation requires the detection of multiple surface electromyograms. *Exerc Sport Sci Rev* 49: 23–34, 2021. doi:10.1249/JES.0000000000000240.
40. **Borzelli D**, **Gazzoni M**, **Botter A**, **Gastaldi L**, **d'Avella A**, **Vieira TM.** Contraction level, but not force direction or wrist position, affects the spatial distribution of motor unit recruitment in the biceps brachii muscle. *Eur J Appl Physiol* 120: 853–860, 2020. doi:10.1007/s00421-020-04324-6.
41. **Borzelli D**, **Gurgone S**, **De Pasquale P**, **Lotti N**, **d'Avella A**, **Gastaldi L.** Use of surface electromyography to estimate end-point force in redundant systems: comparison between linear approaches. *Bioengineering* 10: 234, 2023. doi:10.3390/bioengineering10020234.
42. **Del Vecchio A**, **Holobar A**, **Falla D**, **Felici F**, **Enoka RM**, **Farina D.** Tutorial: Analysis of motor unit discharge characteristics from high-density surface EMG signals. *J Electromyogr Kinesiol* 53: 102426, 2020. doi:10.1016/j.jelekin.2020.102426.
43. **Holobar A**, **Minetto MA**, **Farina D.** Accurate identification of motor unit discharge patterns from high-density surface EMG and validation with a novel signal-based performance metric. *J Neural Eng* 11: 016008, 2014. doi:10.1088/1741-2560/11/1/016008.
44. **Cohen JW**, **Vieira TM**, **Ivanova TD**, **Garland SJ.** Differential behavior of distinct motoneuron pools that innervate the triceps surae. *J Neurophysiol* 129: 272–284, 2023. doi:10.1152/jn.00336.2022.
45. **Power KE**, **Lockyer EJ**, **Botter A**, **Vieira T**, **Button DC.** Endurance-exercise training adaptations in spinal motoneurones: potential functional relevance to locomotor output and assessment in humans. *Eur J Appl Physiol* 122: 1367–1381, 2022. doi:10.1007/s00421-022-04918-2.
46. **Nordstrom MA**, **Fuglevand AJ**, **Enoka RM.** Estimating the strength of common input to human motoneurons from the cross-correlogram. *J Physiol* 453: 547–574, 1992. doi:10.1113/jphysiol.1992.sp019244.
47. **Semmler JG**, **Nordstrom MA.** A comparison of cross-correlation and surface EMG techniques used to quantify motor unit synchronization in humans. *J Neurosci Methods* 90: 47–55, 1999. doi:10.1016/S0165-0270(99)00069-2.
48. **Hug F**, **Avrillon S**, **Sarcher A**, **Del Vecchio A**, **Farina D.** Correlation networks of spinal motor neurons that innervate lower limb muscles during a multi-joint isometric task. *J Physiol* 601: 3201–3219, 2022. doi:10.1113/JP283040.
49. **Negro F**, **Farina D.** Factors influencing the estimates of correlation between motor unit activities in humans. *PLoS One* 7: e44894, 2012. doi:10.1371/journal.pone.0044894.
50. **De Luca CJ**, **Erim Z.** Common drive in motor units of a synergistic muscle pair. *J Neurophysiol* 87: 2200–2204, 2002. doi:10.1152/jn.00793.2001.
51. **Rosenberg JR**, **Amjad AM**, **Breeze P**, **Brillinger DR**, **Halliday DM.** The Fourier approach to the identification of functional coupling between neuronal spike trains. *Prog Biophys Mol Biol* 53: 1–31, 1989. doi:10.1016/0079-6107(89)90004-7.
52. **Semmler JG**, **Kornatz KW**, **Enoka RM.** Motor-unit coherence during isometric contractions is greater in a hand muscle of older adults. *J Neurophysiol* 90: 1346–1349, 2003. doi:10.1152/jn.00941.2002.
53. **Semmler JG**, **Sale MV**, **Meyer FG**, **Nordstrom MA.** Motor-unit coherence and its relation with synchrony are influenced by training. *J Neurophysiol* 92: 3320–3331, 2004. doi:10.1152/jn.00316.2004.
54. **Del Vecchio A**, **Germer CM**, **Elias LA**, **Fu Q**, **Fine J**, **Santello M**, **Farina D.** The human central nervous system transmits common synaptic inputs to distinct motor neuron pools during non-synergistic digit actions. *J Physiol* 597: 5935–5948, 2019. doi:10.1113/JP278623.
55. **De Luca CJ**, **Contessa P.** Biomechanical benefits of the onion-skin motor unit control scheme. *J Biomech* 48: 195–203, 2015. doi:10.1016/j.jbiomech.2014.12.003.
56. **Henneman E.** Relation between size of neurons and their susceptibility to discharge. *Science* 126: 1345–1347, 1957. doi:10.1126/science.126.3287.1345.
57. **Farina D**, **Negro F**, **Dideriksen JL.** The effective neural drive to muscles is the common synaptic input to motor neurons. *J Physiol* 592: 3427–3441, 2014. doi:10.1113/jphysiol.2014.273581.
58. **Castronovo AM**, **Negro F**, **Conforto S**, **Farina D.** The proportion of common synaptic input to motor neurons increases with an increase in net excitatory input. *J Appl Physiol (1985)* 119: 1337–1346, 2015. doi:10.1152/japplphysiol.00255.2015.
59. **Witte M**, **Patino L**, **Andrykiewicz A**, **Hepp-Reymond M-C**, **Kristeva R.** Modulation of human corticomuscular beta-range coherence with low-level static forces. *Eur J Neurosci* 26: 3564–3570, 2007. doi:10.1111/j.1460-9568.2007.05942.x.
60. **Faes L**, **Pinna GD**, **Porta A**, **Maestri R**, **Nollo G.** Surrogate data analysis for assessing the significance of the coherence function. *IEEE Trans Biomed Eng* 51: 1156–1166, 2004. doi:10.1109/TBME.2004.827271.
61. **Freund HJ.** Motor unit and muscle activity in voluntary motor control. *Physiol Rev* 63: 387–436, 1983. doi:10.1152/PHYSREV.1983.63.2.387.
62. **Dideriksen JL**, **Negro F**, **Falla D**, **Kristensen SR**, **Mrachacz-Kersting N**, **Farina D.** Coherence of the surface EMG and common synaptic input to motor neurons. *Front Hum Neurosci* 12: 207, 2018. doi:10.3389/fnhum.2018.00207.
63. **Farina D**, **Merletti R**, **Enoka RM.** The extraction of neural strategies from the surface EMG: an update. *J Appl Physiol (1985)* 117: 1215–1230, 2014. doi:10.1152/japplphysiol.00162.2014.
64. **Negro F**, **Holobar A**, **Farina D.** Fluctuations in isometric muscle force can be described by one linear projection of low-frequency components of motor unit discharge rates. *J Physiol* 587: 5925–5938, 2009. doi:10.1113/jphysiol.2009.178509.
65. **DeFreitas JM**, **Costa PB**, **Ryan ED**, **Herda TJ**, **Cramer JT**, **Beck TW.** An examination of innervation zone movement with increases in isometric torque production. *Clin Neurophysiol* 119: 2795–2799, 2008. doi:10.1016/j.clinph.2008.09.021.
66. **Piitulainen H**, **Rantalainen T**, **Linnamo V**, **Komi P**, **Avela J.** Innervation zone shift at different levels of isometric contraction in the biceps brachii muscle. *J Electromyogr Kinesiol* 19: 667–675, 2009. doi:10.1016/j.jelekin.2008.02.007.
67. **Del Vecchio A**, **Germer C**, **Kinfe TM**, **Nuccio S**, **Hug F**, **Eskofier B**, **Farina D**, **Enoka RM.** Common synaptic inputs are not distributed homogeneously among the motor neurons that innervate synergistic muscles (Preprint). bioRxiv, 2022. doi:10.1101/2022.01.23.477379.
68. **Hug F**, **Avrillon S**, **Ibáñez J**, **Farina D.** Common synaptic input, synergies and size principle: control of spinal motor neurons for movement generation. *J Physiol* 601: 11–20, 2023. doi:10.1113/JP283698.
69. **Hug F**, **Del Vecchio A**, **Avrillon S**, **Farina D**, **Tucker K.** Muscles from the same muscle group do not necessarily share common drive: evidence from the human triceps surae. *J Appl Physiol (1985)* 130: 342–354, 2021. doi:10.1152/japplphysiol.00635.2020.
70. **Negro F**, **Farina D.** Decorrelation of cortical inputs and motoneuron output. *J Neurophysiol* 106: 2688–2697, 2011. doi:10.1152/jn.00336.2011.
71. **Day BL**, **Marsden CD**, **Obeso JA**, **Rothwell JC.** Reciprocal inhibition between the muscles of the human forearm. *J Physiol* 349: 519–534, 1984. doi:10.1113/jphysiol.1984.sp015171.
72. **Lundberg A**, **Voorhoeve P.** Effects from the pyramidal tract on spinal reflex arcs. *Acta Physiol Scand* 56: 201–219, 1962. doi:10.1111/j.1748-1716.1962.tb02498.x.
73. **Nielsen JB.** Sensorimotor integration at spinal level as a basis for muscle coordination during voluntary movement in humans. *J Appl Physiol (1985)* 96: 1961–1967, 2004. doi:10.1152/japplphysiol.01073.2003.
74. **Nielsen J**, **Pierrot-Deseilligny E.** Evidence of facilitation of soleus-coupled Renshaw cells during voluntary co-contraction of antagonistic ankle muscles in man. *J Physiol* 493: 603–611, 1996. doi:10.1113/jphysiol.1996.sp021407.
75. **Shindo M**, **Harayama H**, **Kondo K**, **Yanagisawa N**, **Tanaka R.** Changes in reciprocal Ia inhibition during voluntary contraction in man. *Exp Brain Res* 53: 400–408, 1984. doi:10.1007/BF00238170.
76. **Nielsen J**, **Kagamihara Y.** The regulation of disynaptic reciprocal Ia inhibition during co-contraction of antagonistic muscles in man. *J Physiol* 456: 373–391, 1992. doi:10.1113/jphysiol.1992.sp019341.
77. **Nielsen J**, **Petersen N**, **Deuschl G**, **Ballegaard M.** Task-related changes in the effect of magnetic brain stimulation on spinal neurones in man. *J Physiol* 471: 223–243, 1993. doi:10.1113/jphysiol.1993.sp019899.

78. **Nielsen Y**, **Kagamihara J.** The regulation of presynaptic inhibition during co-contraction of antagonistic muscles in man. *J Physiol* 464: 575–593, 1993. doi:10.1113/jphysiol.1993.sp019652.
79. **Babadi S**, **Vahdat S**, **Milner TE.** Neural substrates of muscle co-contraction during dynamic motor adaptation. *J Neurosci* 41: 5667–5676, 2021. doi:10.1523/JNEUROSCI.2924-19.2021.
80. **Hansen S**, **Hansen NL**, **Christensen LOD**, **Petersen NT**, **Nielsen JB.** Coupling of antagonistic ankle muscles during co-contraction in humans. *Exp Brain Res* 146: 282–292, 2002. doi:10.1007/s00221-002-1152-3.
81. **Nandi T**, **Hortobágyi T**, **van Keeken HG**, **Salem GJ**, **Lamoth CJC.** Standing task difficulty related increase in agonist-agonist and agonist-antagonist common inputs are driven by corticospinal and subcortical inputs respectively. *Sci Rep* 9: 2439, 2019. doi:10.1038/s41598-019-39197-z.
82. **Ohtsuka H**, **Nakajima T**, **Komiyama T**, **Suzuki S**, **Irie S**, **Ariyasu R.** Execution of natural manipulation in the air enhances the β-rhythm intermuscular coherences of the human arm depending on muscle pairs. *J Neurophysiol* 127: 946–957, 2022. doi:10.1152/jn.00421.2021.
83. **Kirkwood PA**, **Sears TA**, **Stagg D**, **Westgaard RH.** The spatial distribution of synchronization of intercostal motoneurones in the cat. *J Physiol* 327: 137–155, 1982. doi:10.1113/jphysiol.1982.sp014224.
84. **Dal Maso F**, **Longcamp M**, **Cremoux S**, **Amarantini D.** Effect of training status on β-range corticomuscular coherence in agonist vs. antagonist muscles during isometric knee contractions. *Exp Brain Res* 235: 3023–3031, 2017. doi:10.1007/s00221-017-5035-z.
85. **Watanabe RN**, **Kohn AF.** Fast oscillatory commands from the motor cortex can be decoded by the spinal cord for force control. *J Neurosci* 35: 13687–13697, 2015. doi:10.1523/JNEUROSCI.1950-15.2015.
86. **Mannard A**, **Stein RB.** Determination of the frequency response of isometric soleus muscle in the cat using random nerve stimulation. *J Physiol* 229: 275–296, 1973. doi:10.1113/jphysiol.1973.sp010138.
87. **Bräcklein M**, **Barsakcioglu DY**, **Vecchio AD**, **Ibáñez J**, **Farina D.** Reading and modulating cortical β bursts from motor unit spiking activity. *J Neurosci* 42: 3611–3621, 2022. doi:10.1523/JNEUROSCI.1885-21.2022.
88. **Zicher B**, **Ibáñez J**, **Farina D.** Beta inputs to motor neurons do not directly contribute to volitional force modulation. *J Physiol* 601: 3173–3185, 2022. doi:10.1113/JP283398.
89. **Ritterband-Rosenbaum A**, **Herskind A**, **Li X**, **Willerslev-Olsen M**, **Damgaard Olsen M**, **Farmer SF**, **Nielsen JB**, **Nielsen JB.** A critical period of corticomuscular and EMG-EMG coherence detection in healthy infants aged 9–25 weeks. *J Physiol* 595: 2699–2713, 2017. doi:10.1113/JP273090.
90. **Lacquaniti F**, **Zago M**, **Farina D.** Tick-tock, spinal motor neurons go with the cortical clock in young infants. *J Physiol* 595: 2405–2406, 2017. doi:10.1113/JP273901.
91. **Herrmann U**, **Flanders M.** Directional tuning of single motor units. *J Neurosci* 18: 8402–8416, 1998. doi:10.1523/JNEUROSCI.18-20-08402.1998.
92. **Hodson-Tole EF**, **Loram ID**, **Vieira TMM.** Myoelectric activity along human gastrocnemius medialis: different spatial distributions of postural and electrically elicited surface potentials. *J Electromyogr Kinesiol* 23: 43–50, 2013. doi:10.1016/j.jelekin.2012.08.003.
93. **ter Haar Romeny BM**, **van der Gon JJ**, **Gielen CC.** Relation between location of a motor unit in the human biceps brachii and its critical firing levels for different tasks. *Exp Neurol* 85: 631–650, 1984. doi:10.1016/0014-4886(84)90036-0.
94. **Borzelli D**, **Berger DJ**, **Pai DK**, **d'Avella A.** Effort minimization and synergistic muscle recruitment for three-dimensional force generation. *Front Comput Neurosci* 7: 186, 2013. doi:10.3389/fncom.2013.00186.
95. **d'Avella A**, **Portone A**, **Fernandez L**, **Lacquaniti F.** Control of fast-reaching movements by muscle synergy combinations. *J Neurosci* 26: 7791–7810, 2006. doi:10.1523/JNEUROSCI.0830-06.2006.
96. **Dominici N**, **Ivanenko YP**, **Cappellini G**, **d'Avella A**, **Mondì V**, **Cicchese M**, **Fabiano A**, **Silei T**, **Di Paolo A**, **Giannini C**, **Poppele RE**, **Lacquaniti F.** Locomotor primitives in newborn babies and their development. *Science* 334: 997–999, 2011. doi:10.1126/science.1210617.
97. **Giszter S**, **Patil V**, **Hart C.** Primitives, premotor drives, and pattern generation: a combined computational and neuroethological perspective. *Prog Brain Res* 165: 323–346, 2007. doi:10.1016/S0079-6123(06)65020-6.
98. **Hart CB**, **Giszter SF.** A neural basis for motor primitives in the spinal cord. *J Neurosci* 30: 1322–1336, 2010. doi:10.1523/JNEUROSCI.5894-08.2010.
99. **Overduin SA**, **d'Avella A**, **Carmena JM**, **Bizzi E.** Microstimulation activates a handful of muscle synergies. *Neuron* 76: 1071–1077, 2012. doi:10.1016/j.neuron.2012.10.018.
100. **Torres-Oviedo G**, **Ting LH.** Subject-specific muscle synergies in human balance control are consistent across different biomechanical contexts. *J Neurophysiol* 103: 3084–3098, 2010. doi:10.1152/jn.00960.2009.
101. **Tanzarella S**, **Muceli S**, **Santello M**, **Farina D.** Synergistic Organization of neural inputs from spinal motor neurons to extrinsic and intrinsic hand muscles. *J Neurosci* 41: 6878–6891, 2021. doi:10.1523/JNEUROSCI.0419-21.2021.
102. **Zandvoort CS**, **van Dieën JH**, **Dominici N**, **Daffertshofer A.** The human sensorimotor cortex fosters muscle synergies through cortico-synergy coherence. *NeuroImage* 199: 30–37, 2019. doi:10.1016/j.neuroimage.2019.05.041.
103. **Ajoudani A**, **Tsagarakis NG**, **Bicchi A.** Tele-impedance: towards transferring human impedance regulation skills to robots. *2012 IEEE International Conference on Robotics and Automation*. Saint Paul, MN, 2012, p. 382–388.
104. **Borzelli D**, **Burdet E**, **Pastorelli S**, **d'Avella A**, **Gastaldi L.** Identification of the best strategy to command variable stiffness using electromyographic signals. *J Neural Eng* 17: 016058, 2020. doi:10.1088/1741-2552/ab6d88.
105. **Borzelli D**, **Pastorelli S**, **Gastaldi L.** Model of the human arm stiffness exerted by two antagonist muscles. In: *Advances in Robot Design and Intelligent Control*, edited by Rodić A, Borangiu T**.** Cham, Switzerland: Springer International Publishing, 2017, p. 285–292.
106. **Borzelli D**, **Pastorelli S**, **Gastaldi L.** Determination of the human arm stiffness efficiency with a two antagonist muscles model. In: *Advances in Italian Mechanism Science*, edited by Boschetti G, Gasparetto A**.** Cham, Switzerland: Springer International Publishing, 2017, p. 71–78.
107. **Abdi E**, **Burdet E**, **Bouri M**, **Himidan S**, **Bleuler H.** In a demanding task, three-handed manipulation is preferred to two-handed manipulation. *Sci Rep* 6: 21758, 2016. doi:10.1038/srep21758.
108. **Salvietti G**, **Hussain I**, **Cioncoloni D**, **Taddei S**, **Rossi S**, **Prattichizzo D.** Compensating hand function in chronic stroke patients through the robotic sixth finger. *IEEE Trans Neural Syst Rehabil Eng* 25: 142–150, 2017. doi:10.1109/TNSRE.2016.2529684.
109. **Dominijanni G**, **Shokur S**, **Salvietti G**, **Buehler S**, **Palmerini E**, **Rossi S**, **De Vignemont F**, **d'Avella A**, **Makin TR**, **Prattichizzo D**, **Micera S.** The neural resource allocation problem when enhancing human bodies with extra robotic limbs. *Nat Mach Intell* 3: 850–860, 2021. doi:10.1038/s42256-021-00398-9.
110. **Eden J**, **Bräcklein M**, **Ibáñez J**, **Barsakcioglu DY**, **Di Pino G**, **Farina D**, **Burdet E**, **Mehring C.** Principles of human movement augmentation and the challenges in making it a reality. *Nat Commun* 13: 1345, 2022. doi:10.1038/s41467-022-28725-7.
111. **Lisini Baldi T**, **D'Aurizio N**, **Gurgone S**, **Borzelli D**, **D'Avella A**, **Prattichizzo D.** Exploiting intrinsic kinematic null space for supernumerary robotic limbs control. *2023 IEEE International Conference on Robotics and Automation (ICRA)*. London, UK, 2023, p. 11957–11963.
112. **Bräcklein M**, **Ibáñez J**, **Barsakcioglu DY**, **Farina D.** Towards human motor augmentation by voluntary decoupling beta activity in the neural drive to muscle and force production. *J Neural Eng* 18: 016001, 2021. doi:10.1088/1741-2552/abcdbf.
113. **Rosa MCN**, **Marques A**, **Demain S**, **Metcalf CD.** Lower limb co-contraction during walking in subjects with stroke: a systematic review. *J Electromyogr Kinesiol* 24: 1–10, 2014. doi:10.1016/j.jelekin.2013.10.016.
114. **Malfait N**, **Sanger TD.** Does dystonia always include co-contraction? A study of unconstrained reaching in children with primary and secondary dystonia. *Exp Brain Res* 176: 206–216, 2007. doi:10.1007/s00221-006-0606-4.
115. **Fung VSC**, **Burne JA**, **Morris JGL.** Objective quantification of resting and activated parkinsonian rigidity: a comparison of angular impulse and work scores. *Mov Disord* 15: 48–55, 2000. doi:10.1002/1531-8257(200001)15:1<48::AID-MDS1009>3.0.CO;2-E.